



1 **Tropical tropospheric ozone distribution and trends from in situ and satellite**
2 **data**

3

4

5 **Audrey Gaudel^{1,2*}, Ilann Bourgeois^{1,2,#}, Meng Li^{1,2}, Kai-Lan Chang^{1,2}, Jerald Ziemke^{3,4},**
6 **Bastien Sauvage⁵, Ryan M. Stauffer³, Anne M. Thompson^{3,6}, Debra E. Kollonige^{3,7}, Nadia**
7 **Smith⁸, Daan Hubert⁹, Arno Keppens⁹, Juan Cuesta¹⁰, Klaus-Peter Heue¹¹, Pepijn**
8 **Veefkind^{12,13}, Kenneth Aikin^{1,2}, Jeff Peischl^{1,2}, Chelsea R. Thompson², Thomas B. Ryerson²,**
9 **Gregory J. Frost², Brian C. McDonald², Owen R. Cooper^{1,2}**

10

11 ¹**CIRES, University of Colorado, Boulder, USA**

12 ²**NOAA Chemical Sciences Laboratory, Boulder, USA**

13 ³**NASA Goddard Space Flight Center, Greenbelt, Maryland, USA**

14 ⁴**Morgan State University, Baltimore, Maryland, USA**

15 ⁵**Laboratoire d'Aérodologie, Université de Toulouse, CNRS, Université Toulouse III Paul**
16 **Sabatier, France**

17 ⁶**University of Maryland Baltimore County, Baltimore, MD, USA**

18 ⁷**Science Systems and Applications, Inc., Lanham, MD, USA**

19 ⁸**Science and Technology Corporation, Madison, Wisconsin, 53703, USA**

20 ⁹**Royal Belgian Institute for Space Aeronomy (BIRA-IASB), 1180 Brussels, Belgium**

21 ¹⁰**Laboratoire Inter-universitaire des Systèmes Atmosphériques (LISA), UMR7583,**
22 **Universités Paris-Est Créteil et Paris, Diderot, CNRS, Créteil, FR**

23 ¹¹**Technische Universität München (TUM), School of Engineering and design, and**
24 **Deutsches Zentrum für Luft- und Raumfahrt (DLR), Institut für Methodik der**
25 **Fernerkundung (IMF), Oberpfaffenhofen, Germany**

26 ¹²**Royal Netherlands Meteorological Institute, De Bilt, 3731 GA, the Netherlands**

27 ¹³**Faculty of Civil Engineering and Geosciences, University of Technology Delft, Delft, 2628**
28 **CN, the Netherlands**

29 [#]**Now at University Savoie Mont Blanc, INRAE, CARTELE, F-74200 Thonon-les-Bains,**
30 **France**

31 ***Correspondence: audrey.gaudel@noaa.gov**

32



33 **Abstract**

34 Tropical tropospheric ozone (TTO) is important for the global radiation budget because the
35 longwave radiative effect of tropospheric ozone is higher in the tropics than mid-latitudes. In
36 recent decades the TTO burden has increased, partly due to the ongoing shift of ozone precursor
37 emissions from mid-latitude regions toward the equator. In this study, we assess the distribution
38 and trends of TTO using ozone profiles measured by high quality in situ instruments from the
39 IAGOS (In-Service Aircraft for a Global Observing System) commercial aircraft, the SHADOZ
40 (Southern Hemisphere ADditional OZonesondes) network, and the ATom (Atmospheric
41 Tomographic Mission) aircraft campaign, as well as six satellite records reporting tropical
42 tropospheric column ozone (TTCO): TROPOMI, OMI, OMI/MLS, OMPS/MERRA2, CrIS, and
43 IASI/GOME2. With greater availability of ozone profiles across the tropics we can now
44 demonstrate that tropical India is among the most polluted regions (e.g., Western Africa, tropical
45 South Atlantic, Southeast Asia, Malaysia/Indonesia) with present-day 95th percentile ozone
46 values reaching 80 nmol mol⁻¹ in the lower free troposphere, comparable to mid-latitude regions
47 such as Northeast China/Korea. In situ observations show that TTO increased between 1994 and
48 2019, with the largest mid- and upper tropospheric increases above India, Southeast Asia and
49 Malaysia/Indonesia (from 3.4 ± 0.8 to 6.8 ± 1.8 nmol mol⁻¹ decade⁻¹), reaching 11 ± 2.4 and $8 \pm$
50 0.8 nmol mol⁻¹ decade⁻¹ close to the surface (India and Malaysia/Indonesia, respectively). The
51 longest continuous satellite records only span 2004-2019, but also show increasing ozone across
52 the tropics when their full sampling is considered, with maximum trends over Southeast Asia of
53 2.31 ± 1.34 nmol mol⁻¹ decade⁻¹ (OMI) and 1.69 ± 0.89 nmol mol⁻¹ decade⁻¹ (OMI/MLS). In
54 general, the sparsely sampled aircraft and ozonesonde records do not detect the 2004-2019 ozone
55 increase, which could be due to the genuine trends on this timescale being masked by the
56 additional uncertainty resulting from sparse sampling. The fact that the sign of the trends
57 detected with satellite records changes above three IAGOS regions, when their sampling
58 frequency is limited to that of the in situ observations, demonstrates the limitations of sparse in
59 situ sampling strategies. This study exposes the need to maintain and develop high frequency
60 continuous observations (in situ and remote sensing) above the tropical Pacific Ocean, the Indian
61 Ocean, Western Africa and South Asia in order to estimate accurate and precise ozone trends for
62 these regions. In contrast, Southeast Asia and Malaysia/Indonesia are regions with such strong
63 increases of ozone that the current in situ sampling frequency is adequate to detect the trends on
64 a relatively short 15-year time scale.

65

66 **Plain Language Summary**

67 Tropospheric ozone is an air pollutant and a climate forcer, and plays an important role in the
68 global Earth's radiation budget, especially in the tropics. In recent decades, the tropical
69 tropospheric ozone burden has increased, partly due to the ongoing shift of ozone precursor
70 emissions from mid-latitudes toward the equator. In this study, we assess the changes in time of
71 tropical tropospheric ozone using in situ ozone profiles measured by high quality instruments
72 from commercial aircraft, ozonesondes and satellites. In situ observations show that tropical
73 tropospheric ozone increased between 1994 and 2019, with the largest increases above India,
74 Southeast Asia and Malaysia/Indonesia. The longest continuous satellite records of ozone only
75 span 2004-2019, but show increasing ozone across the tropics, with maximum trends over



76 Southeast Asia. In general, the sparsely sampled aircraft and ozonesonde records do not detect
77 the 2004-2019 ozone increase, which could be due to sample sizes that are too small for accurate
78 trend detection on this relatively short 15-year time period. The fact that the satellite records also
79 fail to consistently detect positive trends when their sampling frequency is limited to that of the
80 in situ observations demonstrates the limitations of sparse in situ sampling in the tropics. This
81 study demonstrates the need to maintain and develop continuous observations (in situ and remote
82 sensing) above the tropical Pacific Ocean, the Indian Ocean, Western Africa and South Asia in
83 order to estimate accurate and precise ozone trends for these regions.

84

85 **Short Summary (500 characters)**

86 The study examines tropical tropospheric ozone changes. In situ data from 1994-2019 display
87 increased ozone, notably over India, Southeast Asia, and Malaysia/Indonesia. Sparse in situ data
88 limit trend detection for the 15-year period. In situ and satellite data, with limited sampling,
89 struggle to consistently detect trends. Continuous observations are vital over the tropical Pacific
90 Ocean, Indian Ocean, Western Africa, and South Asia for accurate ozone trend estimation in
91 these regions.

92

93

94

95

96

97

98 **1. Introduction**

99 Tropospheric ozone negatively affects human health and vegetation, and it is a short-lived
100 climate forcer (Fleming et al., 2018; Mills et al., 2018; Gulev et al., 2022; Szopa et al., 2022).
101 The longwave radiative effect of tropospheric ozone is higher in the tropics and subtropics
102 (between 30°S and 30°N) compared to mid-latitudes (Doniki et al., 2015; Gaudel et al., 2018).
103 The most recent IPCC assessment concluded with a high level of confidence that tropical ozone
104 increased by 2-17% per decade in the lower troposphere, and by 2-12% per decade in the free
105 troposphere from the mid-1990s to the period 2015-2018 (Gulev et al., 2021). These increases
106 are especially strong across southern Asia (Gaudel et al., 2020), and according to the longest
107 available satellite record, ozone increases in this region have been occurring since at least 1979
108 (Ziemke et al., 2019). A comprehensive NASA analysis used the OMI/MLS satellite record to
109 show a clear increase of tropospheric column ozone (1-2.5 DU decade⁻¹) between 2005 and 2016
110 throughout the tropics, with larger trends over the Arabian Peninsula, India and Southeast Asia,
111 generally consistent with a simulation by NASA's MERRA-2 GMI global atmospheric
112 chemistry model (Ziemke et al., 2019). Similar results were found in a recent study using the
113 NASA Goddard Earth Observing System Chemistry Climate Model (Liu et al., 2022). Weak to
114 moderate positive trends of 0.6 and 1.5 nmol mol⁻¹ decade⁻¹ between 1995 and 2015-2018 were
115 also reported at two remote tropical surface sites (Mauna Loa, Hawaii, and American Samoa,
116 South Pacific; Cooper et al., 2020). A recent analysis of 1998-2019 tropical ozone trends using
117 the Southern Hemisphere ADditional OZonesondes (SHADOZ) network reported highly



118 seasonal but overall weak positive trends (1-2% decade⁻¹) in the mid-troposphere (5-10 km)
119 (Thompson et al., 2021).

120 Simulations by a wide range of global atmospheric chemistry models show that global-
121 scale increases of tropospheric ozone since pre-industrial times are driven by anthropogenic
122 emissions of ozone precursor gases (Archibald et al., 2020; Skeie et al., 2020; Griffiths et al.,
123 2021; Szopa et al., 2021; Wang et al., 2022; Fiore et al. 2022), with approximately 54% of the
124 1850-2000 global tropospheric ozone increase occurring in the tropics (30° S – 30° N) (Young et
125 al., 2013). A key ozone precursor that drives the background increase of tropospheric ozone,
126 especially in the free troposphere is methane (Thompson and Cicerone, 1986a,b; Hogan et al.,
127 1991; Fiore et al., 2002). From 1980 to 2010 the estimated increase of the global tropospheric
128 ozone burden due to the increase of anthropogenic emissions and the partial shift of the
129 emissions from mid-latitudes towards the equator was 28.12 Tg (8.9%), with the increase of
130 methane (15%) accounting for one quarter of the ozone burden increase (as simulated by the
131 CAM-chem model; Zhang et al., 2016). Most of the ozone burden increase (64%) occurred in the
132 tropics (30° S – 30° N), driven by emissions from South Asia, Southeast Asia and by increasing
133 background methane levels (Zhang et al., 2021). Similar rates of ozone burden increases,
134 peaking in the tropics, are simulated by a range of CMIP6 models (1995-2014) (Skeie et al.,
135 2020,) the GEOS-Chem model (1995-2017) (Wang et al., 2022), the JPL TCR-2 chemical
136 reanalysis (1995-2018) (Miyazaki et al., 2020), and a 15-member initial-condition ensemble
137 generated from the CESM2-WACCM6 chemistry-climate model (1950-2014) (Fiore et al.,
138 2022). The increase of methane has continued to the present and the observed global mean
139 methane increase from 1983 to 2023 is 18% (the increase is 8% since 2004 when the OMI
140 satellite instrument began operations) (www.gml.noaa.gov). Under a future scenario of high
141 anthropogenic emissions and continuously increasing methane concentrations (Griffiths et al.,
142 2021), the global ozone burden is expected to increase for the remainder of the 21st century (see
143 the ssp370 scenario in Figure 6.4 of Szopa et al., 2021), with increases of approximately 10%
144 from 2014 to 2050. In the tropics the strongest increases (though 2050) are expected across
145 South Asia (10-20%), with little or no increase across the remote regions of the equatorial Pacific
146 and equatorial Atlantic.

147 The tropics are characterized by high ozone values over the southern tropical Atlantic and
148 Southeast Asia (Fishman et al., 1990; Fishman et al., 1996; Thompson et al., 1996; Logan et al.,
149 1999; Ziemke et al., 2019) and low ozone values (< 10 nmol mol⁻¹) in the free troposphere over
150 the Pacific warm pool (Kley et al., 1996), although these low values have become less frequent
151 over the last two decades (Gaudel et al., 2020). The spatial distribution of tropical tropospheric
152 ozone (TTO) can vary on a range of timescales. On multi-year timescales TTO experiences a
153 dipole oscillation across the tropical Pacific Ocean due to El Niño-Southern Oscillation (ENSO)
154 (Chandra et al., 1998; Doherty et al., 2006; Oman et al., 2013; Xue et al., 2020). On seasonal
155 time scales ozone can vary with the Madden-Julian Oscillation (MJO) (Ziemke et al., 2015), and
156 also with dry and wet conditions (a.k.a. biomass burning and monsoon seasons) related to the
157 seasonal shifts of the Intertropical Convergence Zone (ITCZ) (Fishman et al., 1992; Oltmans et
158 al., 2001; Sauvage et al., 2007; Thompson et al., 2012). In a given season, TTO can be further
159 influenced by biomass burning, lightning, inter-hemispheric transport and stratospheric
160 intrusions/large-scale subsidence (Sauvage et al., 2007; Jenkins et al., 2014; Yamasoe et al.,



161 2015; Hubert et al., 2021). For instance, high ozone concentrations were recently measured
162 above the tropical Atlantic (Bourgeois et al., 2020), and were attributed to biomass burning
163 emissions, whose effects on tropospheric ozone enhancements are underestimated by global
164 chemistry-transport models, especially in the tropics and the southern hemisphere (Bourgeois et
165 al., 2021).

166 While decades of research on the distribution of TTO using satellite instruments (Fishman
167 et al., 1986, 1987, 1990; Ziemke et al., 1998, 2005, 2009, 2011, 2019) and in situ observations
168 (Logan et al., 1999; Thompson et al., 2000, 2003, 2012, 2021; Oltmans et al., 2001; Sauvage et
169 al., 2005; Sauvage et al., 2007; Yamasoe et al., 2015; Tarasick et al., 2019; Cooper et al., 2020,
170 Lannuque et al., 2021) have characterized the spatial and temporal variability of TTO
171 concentrations, reconciling differences between satellite and in situ observations has been a
172 challenge (Gaudel et al., 2018).

173 To update our understanding of tropospheric ozone's distribution and trends across the
174 tropics, this study presents a quantitative analysis of four complementary data sets in time and
175 space across the 20°S-20°N latitude band: (1) Thousands of vertical ozone profiles from the In-
176 Service Aircraft for a Global Observing System (IAGOS) (Nédélec et al., 2015; Blot et al., 2021)
177 above five continental regions; (2) Regular vertical profiles from the SHADOZ ozonesonde
178 network (Thompson et al., 2017; Stauffer et al., 2022) above 14 continental and oceanic sites; (3)
179 Vertical profiles from the Atmospheric Tomographic Mission (ATom) aircraft campaign above
180 five oceanic regions; (4) Tropospheric column ozone retrievals from four well-known and two
181 new satellite records.

182 The paper is organized as follows. Section 2 describes the data sets and the methodology
183 for quantifying the distribution and trends of ozone. Section 3 presents the results that include the
184 distribution of ozone from the in situ data, an evaluation of the satellite records and the trend
185 estimates from IAGOS, SHADOZ and satellite records. Section 4 presents the main conclusions.

186

187 **2. Methods**

188 We define the tropics as the latitude band between 20°S and 20°N, within the bounds of
189 the Tropic of Cancer and the Tropic of Capricorn. This latitude band covers most of the Southern
190 Hemisphere ADDitional OZonesondes (SHADOZ) network designed to measure ozone in the
191 subtropics/tropics. The goal of the study is to characterize the 20°S-20°N latitude band that can
192 be impacted by subtropical air masses in some regions, especially at the edge of the domain.
193 The satellite data are shown for the same domain but we also include one satellite record, for
194 which the tropical tropospheric column ozone (TTCO) retrieval is based on the cloud slicing
195 technique, that is limited to 15°N -15°S.

196 We focus on three time periods: 2014-2019, also called “present-day” to assess the
197 distribution of TTO (5th, 50th, and 95th percentiles) with in situ data above the sampled regions
198 and sites described in Figure 1; 1994-2019 to assess ozone trends using in situ data records for
199 more than two decades; 2004-2019 to assess ozone trends over the time period of the Ozone
200 Monitoring Instrument (OMI) data set, which is the longest time series of ozone measured from
201 space from a satellite.

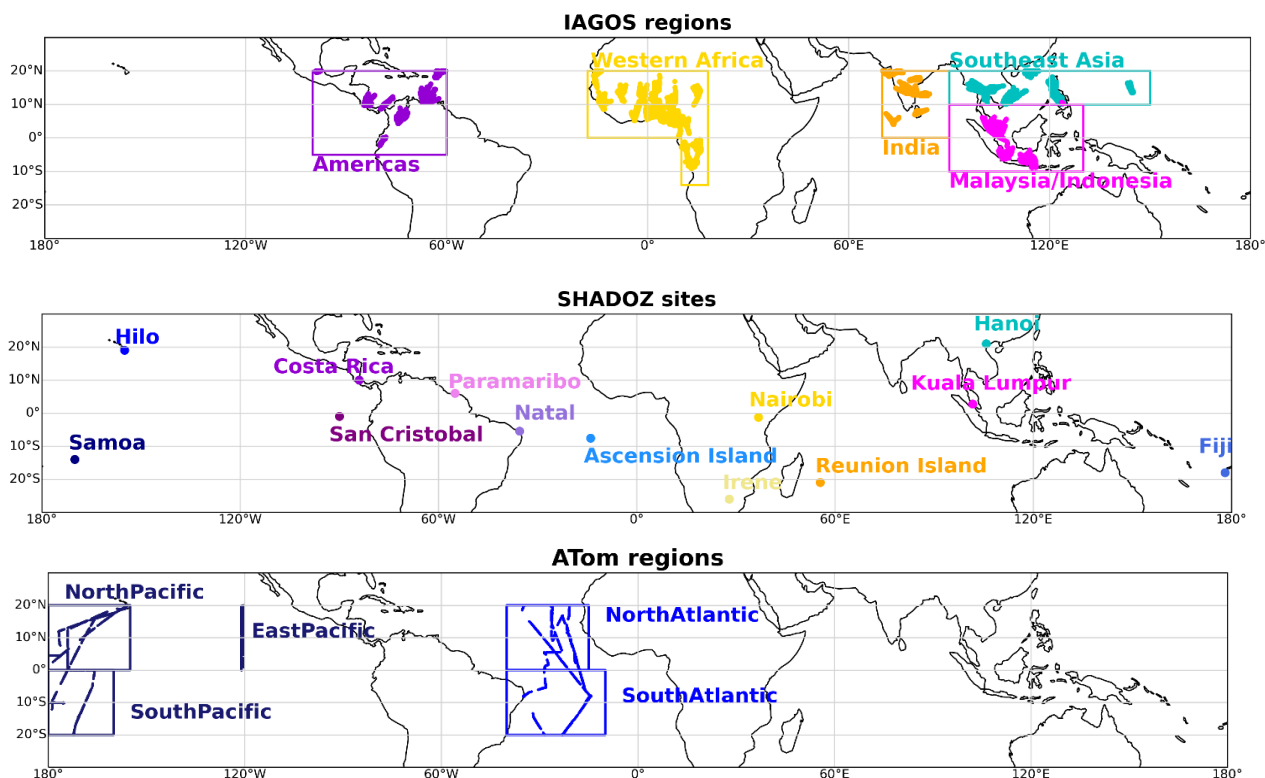
202 We also use new datasets to assess the distribution of TTO, such as the ATom aircraft
203 campaign, and the CrIS and IASI/GOME2 satellite records.



204
205
206

2.1 In situ measurements

207



208

209
210
211
212

Figure 1. Regions and sites of IAGOS, SHADOZ and ATom measurements used in this study to assess the 5th, 50th and 95th percentiles of ozone in the tropical troposphere over 2014-2019. Data from IAGOS and ATom flights are clustered into specific regions such as Americas, Africa, South Asia, Southeast Asia, Malaysia/Indonesia, North Pacific, South Pacific, East Pacific, North Atlantic and South Atlantic. IAGOS and ATom flight tracks are plotted on the map to show the specific sampling locations for 2014-2019. IAGOS and SHADOZ data are statistically fused above the Americas, Southeast Asia and Malaysia/Indonesia and used to estimate ozone trends between 1994 and 2019. For India, only IAGOS data are available for the ozone trend estimate between 1994 and 2019.

2.1.1 IAGOS

Description: The European research infrastructure In-service Aircraft for a Global Observing System (IAGOS), formerly known as the Measurement of Ozone and Water Vapor by Airbus In Service Aircraft (MOZAIC), has collected continuous high quality ozone profiles up to



227 12 km (~ 200 hPa) on-board commercial aircraft since 1994 (Blot et al., 2020). Ozone is
228 measured using a UV analyzer (Thermo Scientific, model 49) and the total uncertainty is ± 2
229 $\text{nmol mol}^{-1} \pm 2\%$ (Nédélec et al., 2015).

230 Data treatment: For this study, we consider five tropical regions: Americas, Africa, India,
231 Southeast Asia and Malaysia/Indonesia. We use IAGOS data to assess the average ozone
232 distribution between 2014 and 2019, referred to as “present-day ozone”, as well as to assess
233 ozone trends between 1994 and 2019. Over the time period 1994-2019, the most frequented
234 airports were Caracas (1214 profiles) and Bogota (560 profiles) for the Americas; Lagos (761
235 profiles) and other airports in the Gulf of Guinea for Western Africa; Chennai (680 profiles) and
236 Hyderabad (552 profiles) for India; Bangkok (1535 profiles) and Ho Chi Minh City (367
237 profiles) for Southeast Asia; Singapore (265 profiles), Kuala Lumpur (208 profiles) and Jakarta
238 (113 profiles) for Malaysia/Indonesia (Table S1). All available ozone profiles from these airports
239 are used in this study. The individual ozone profiles are averaged to a common vertical
240 resolution of 10 hPa prior to any further analysis. To assess the annual ozone distribution the
241 profiles are averaged annually. To assess ozone trends, the quantile regression method is applied
242 to individual profiles (section 2.5). To compare with the satellite data, the profiles were averaged
243 monthly before being converted to a tropospheric column value ranging from the surface up to
244 270 hPa or up to the maximum altitude (~ 200 hPa). We chose 270 hPa to be consistent with the
245 TROPOMI tropical tropospheric column ozone. While some of the satellite records used in this
246 study have an upper limit at 150 hPa (thermal tropopause), IAGOS commercial aircraft do not
247 reach these altitudes.

248

249 2.1.2 SHADOZ

250 Description: The Southern Hemisphere ADDitional OZonesondes (SHADOZ) network
251 has provided ozone profiles at multiple sites between 25°S and 21°N since 1998, and presently
252 operates 14 sites. SHADOZ is a NASA-sponsored project operated by NOAA and 15 institutions
253 around the world (Thompson et al., 2003a, 2003b, 2012, 2021). The SHADOZ archive of ozone
254 profiles, measured by electrochemical concentration cell (ECC) ozonesondes, were reprocessed
255 in 2016-2018 (Witte et al., 2017; 2018). In comparisons of the reprocessed data with collocated
256 total ozone spectrometers and satellite overpasses, the reprocessed SHADOZ total ozone column
257 (TOC) agreed with the independent data to 2% (Thompson et al., 2017). SHADOZ data since
258 2018 have been collected and processed according to the same protocols as the reprocessed
259 profiles (Stauffer et al., 2018, 2020; 2022; WMO/GAW 268, 2021). A recent study of TOC
260 stability over 60 global stations revealed an artifact of declining tropospheric ozone at the
261 SHADOZ Hilo and Costa Rican stations (Stauffer et al., 2020; 2022). Those data were not used
262 in the recent Thompson et al. (2021) study that showed distinctive seasonal and regional
263 variations in ozone trends collected at eight SHADOZ stations within $\pm 15^\circ$ latitude of the
264 equator.

265 Data treatment: As with the IAGOS data, the SHADOZ ozone profiles were averaged to
266 a common vertical resolution of 10 hPa before any further analysis. The 10 hPa-resolution
267 vertical profiles are fused with the IAGOS 10 hPa-resolution vertical profiles to assess trends
268 between the surface and 200 hPa (section 2.6). To compare with the satellite data, the profiles



269 were averaged monthly before being converted to tropospheric columns up to 270 hPa, 150 hPa
270 and 100 hPa.

271

272 **2.1.3 ATom**

273 Description: The Atmospheric Tomography (ATom) project was a global scale NASA
274 aircraft mission which collected profiles of ozone and hundreds of other atmospheric constituents
275 in remote regions above the Atlantic and Pacific basins on board the NASA DC-8 aircraft. The
276 project consisted of four seasonal circumnavigations of the globe, one in each season,
277 continually profiling the troposphere between 180 m and 14 km a.s.l. with a temporal resolution
278 of 10 Hz, averaged to 1 Hz (data available at <https://espo.nasa.gov/atom>, last access March 7,
279 2022). The ATom mission occurred in July–August 2016 (ATom-1), January–February 2017
280 (ATom-2), September– October 2017 (ATom-3), and April–May 2018 (ATom-4). Ozone was
281 measured using the National Oceanic and Atmospheric Administration (NOAA) nitrogen oxides
282 and ozone (NOyO3) instrument (Bourgeois et al. 2020). The total estimated uncertainty at sea
283 level is $\pm (0.015 \text{ nmol mol}^{-1} \pm 2 \%)$.

284 Data treatment: We used the ATom ozone profiles available above five regions in the
285 tropics: North Pacific, South Pacific, East Pacific, North Atlantic and South Atlantic. Most of
286 the regions were sampled over one day in August 2016, February and October 2017, and May
287 2018, except the East Pacific which was sampled in July 2016, January and September 2017, and
288 April 2018. Each flight produced 6-14 profiles in each region. Therefore, the ATom dataset is
289 used to assess the ozone distribution over the 2016-2018 time-period and for the annual
290 comparison with the satellite products. As for IAGOS and SHADOZ, we averaged the profiles to
291 a common vertical resolution of 10 hPa within the five ATom regions. To compare with satellite
292 data, the profiles were converted to tropospheric column ozone from the near-surface
293 measurements up to 270 hPa and averaged for the entire ATom period above each of the five
294 regions.

295

296 **2.2 Tropical Tropospheric Column Ozone (TTCO) estimation from IAGOS, SHADOZ and** 297 **ATom**

298 In this study and as mentioned in Section 2.1, the ozone profiles from in situ observations
299 have been converted to columns to evaluate the satellite products. The current TOAR-II
300 Harmonization and Evaluation of Ground-based Instrument for Free Tropospheric Ozone
301 Measurements (HEGIFTOM) focus working group (<https://hegiftom.meteo.be/>) recommended
302 150 hPa as the top limit of the TTCO in the 15°S-15°N tropical band and 200 hPa in the 15°S-
303 30°S/15°N-30°N bands. As we focus our study on the 20°S-20°N latitude band, we decided to use
304 the 150 hPa top limit. Some variations on the TTCO definition occur in this study and are
305 detailed below, but are not corrected for.

306 IAGOS aircraft cannot reach 150 hPa as they have a maximum cruise altitude around 200
307 hPa. Therefore, only SHADOZ ozonesondes, which reach the mid- or upper stratosphere, were
308 used to calculate TTCO from the surface to 150 hPa. However, we additionally calculated TTCO
309 up to 270 hPa with IAGOS and ATom to compare with TROPospheric Monitoring Instrument
310 (TROPOMI) and Infrared Atmospheric Sounding Interferometer (IASI) / Global Ozone
311 Monitoring Experiment 2 (GOME2) satellite data.



312

313 **2.3 Satellite data**

314 In this study we mainly focus on satellite data based on ultraviolet absorption (UV)
315 retrievals, supplemented with two ozone records derived from infrared (IR) measurements as
316 described below. Two key parameters differ between the satellite datasets: (i) the top limit used
317 to define the tropospheric column ozone, and (ii) the horizontal coverage. Figure S1 shows the
318 time series of the pressure level characterizing the top limit. Depending on the datasets, the top
319 limit is constant or varies with time. The tropical coverage is 20°S-20°N for all satellite records
320 except the Ozone Monitoring Instrument (OMI) data, which is constrained to 15°S-15°N. All
321 satellite records were averaged to a common 5°x5° monthly grid.

322

323 **2.3.1 TROPOMI CCD**

324 The TROPospheric Monitoring Instrument (TROPOMI, Veefkind et al., 2012) was
325 launched onboard the Sentinel-5 Precursor (S5P) satellite in October 2017. The tropospheric
326 column ozone data from TROPOMI, inferred using the convective cloud differential technique
327 (CCD, Ziemke et al., 1998; Heue et al., 2016; Hubert et al., 2021), covers the 20°S-20°N latitude
328 band, between the surface and 270 hPa. For this study, we compute monthly data from daily
329 measurements on a 5° x 5° grid to be consistent with the other satellite data records. For the 5° x
330 5° gridded data we estimate the uncertainty of the TROPOMI CCD tropospheric ozone column
331 to be about 2 DU. We only use data from 2019, which is the last year of our present-day time
332 period 2014-2019.

333

334 **2.3.2 OMI CCD**

335 The Ozone Monitoring Instrument (OMI) was launched onboard the Aura satellite in July
336 2004. For this study we used tropical tropospheric column ozone retrieved using the CCD
337 technique (Ziemke et al., 1998; Ziemke and Chandra, 2012), which is consistent with
338 TROPOMI-derived TCO. The tropospheric column is defined between the surface and 100
339 hPa, and it is constrained in the 15°S-15°N latitude band inherent to the CCD technique. OMI
340 records are available since 2004 and for this study we use monthly means to assess ozone
341 distribution during the present-day time period of 2014-2019 as well as the trends of ozone over
342 2004-2019. The monthly accuracy and precision (1σ) are 3 and 3.5 DU, respectively.

343

344 **2.3.3 OMI/MLS**

345 The OMI and the Microwave Limb Sounder (MLS) sensors are both onboard the Aura
346 satellite and the tropospheric column ozone is retrieved by subtracting the stratospheric column
347 ozone measured by MLS from the total column ozone measured by OMI (Ziemke et al., 2006).
348 The top limit of the OMI/MLS tropospheric column ozone is the thermal tropopause calculated
349 from NCEP reanalysis data using the World Meteorological Organization (WMO) 2 K km^{-1}
350 lapse-rate definition. The tropopause varies seasonally between 95 and 115 hPa (Figure S1).
351 OMI/MLS data cover the 60°S-60°N latitude band and for this study we focus on the 20°S-20°N
352 latitude band. The monthly accuracy and precision (1σ) are 2 and 1.5 DU, respectively. Further
353 details of the OMI/MLS product and a description of an updated drift correction can be found in
354 Section S.2 of the supplementary material.



355

356 **2.3.4 OMPS/MERRA2**

357 The Ozone Mapping Profiler Suite (OMPS) was launched in January 2012 onboard the
358 Suomi National Polar-orbiting Partnership (Suomi NPP) spacecraft. The tropospheric column
359 ozone is retrieved by subtracting the stratospheric column of MERRA2 (Modern-Era
360 Retrospective analysis for Research and Applications, version 2) ozone reanalysis data from the
361 total column ozone of the OMPS nadir mapper (Ziemke et al., 2019). The derived daily
362 tropospheric column ozone uses the MERRA2 tropopause with assimilated MLS ozone. The
363 MERRA2 tropopause was determined using a potential vorticity (PV) – potential temperature (θ)
364 definition (2.5 PV units, 380 K; Wargan et al., 2020). The tropopause at a given grid point was
365 taken as the larger of these two PV and θ surfaces. However, in this study, the tropopause is
366 exclusively defined by θ surfaces as we focus on the 20°S–20°N latitude band. For the MERRA2
367 assimilation, in 2015 MLS changed from version 2.2 to version 4.2 (Wargan et al., 2017; Davis
368 et al., 2017). This produced a 1–1.5 DU difference between the earlier and latter record for
369 stratospheric column ozone, which prevents accurate trend detection from either MERRA2
370 stratospheric column ozone or the derived tropospheric column ozone from OMPS/MERRA2.
371 The OMPS/MERRA 2 tropopause pressure varies seasonally between 95 hPa and 108 hPa
372 (Figure S1). The monthly accuracy and precision (1σ) are 3 and 2 DU, respectively.

373

374 **2.3.5 CrIS**

375 The Cross track Infrared Sounder (CrIS) is onboard the Suomi NPP (2011–2021) and
376 JPSS-1 (NOAA-20 in operations; 2017–present) and builds upon the hyperspectral IR record
377 first started by the Atmospheric Infrared Sounder (AIRS) on Aqua (2002–2022). For this study
378 we are focusing on the ozone profiles retrieved by the Community Long-term Infrared
379 Microwave Combined Atmospheric Product System (CLIMCAPS, Smith and Barnett, 2019;
380 2020). CLIMCAPS retrieves atmospheric state parameters, including ozone profiles (from the
381 surface to the top of the atmosphere), from AIRS and CrIS to form a long-term record that spans
382 instrument and platform differences. CLIMCAPS uses MERRA2 as the a-priori for ozone. Here
383 we focus on CLIMCAPS from CrIS onboard Suomi NPP (National Polar-orbiting Partnership,
384 2016-01-01 to 2018-03-31) and NOAA-20 (previously known as JPSS-1, 2018-04-01 to 2022-
385 08-31) for the time period 2016–2019 because this gives us the baseline IR sounding capability
386 for the next two decades (CrIS is scheduled for launch on three additional JPSS platforms). CrIS
387 data covers the 90°S–90°N latitude band and for this study we focus on the 20°S–20°N latitude
388 band. The accuracy that CrIS vary between -9.4% globally and -20% in the tropics compared
389 with ozonesondes. The precision that CrIS globally is 21.2% (Nalli et al., 2017).

390 For CrIS, we accessed CLIMCAPS Level 2 retrievals via NASA GES DISC (NASA
391 Goddard Earth Sciences Data and Information Services Center; Sounder SIPS, & Barnett, Chris.,
392 2020a and 2020b; <https://disc.gsfc.nasa.gov/>). We aggregated them onto 1° equal angle global
393 grids. Specifically, we accessed the ozone retrieved fields (o3_mol_lay) defined as 100 layer
394 column density profiles [molec m^{-2}] and subset them into tropospheric profiles. We defined the
395 troposphere as all values between Earth surface (prior_surf_pres) and tropopause (tpause_pres).
396 A total column value is simply the sum of all column density values, converted to DU. We used
397 the quality flag (ispare_2=0) to define all successful retrievals, which we simply averaged per



398 grid box. No other filtering was done. CLIMCAPS retrievals are done from cloud cleared
 399 radiances so we do not have to make specific accommodation for clouds.

400

401 **2.3.6 IASI / GOME2**

402 IASI/GOME2 is a multispectral approach used to retrieve ozone for several partial
 403 columns. It is based on the synergism of IASI and GOME-2 measurements respectively in the
 404 thermal infrared and the ultraviolet spectral domain, jointly used in terms of radiance spectra for
 405 enhancing the sensitivity of the retrieval for lowermost tropospheric ozone (below 3 km above
 406 sea level, see Cuesta et al., 2013). Studies over Europe and East Asia have shown good skill for
 407 capturing near surface ozone variability compared to surface in situ measurements of ozone
 408 (Cuesta et al. 2018; 2022). This ozone product offers global coverage for low cloud fraction
 409 conditions (below 30%) for 12-km diameter pixels spaced by 25 km (at nadir pointing). The
 410 IASI/GOME2 global dataset is publicly available through the AERIS French data center, with
 411 data from 2017 to the present (available at https://iasi.aeris-data.fr/o3_iago2/, last accessed
 412 08/02/2023) and covers the 90°S-90°N latitude band. For this study, we are using the 2017-2021
 413 monthly tropospheric column ozone between the surface and 12 km, focusing on the 20°S-20°N
 414 latitude band.

415

416 **2.4 Comparison between satellite and in situ data**

417 To assess the performance of the six satellite records, we calculated the mean biases
 418 between satellite-detected monthly TCO and IAGOS and SHADOZ integrated profiles over the
 419 2014-2019 time period. The biases are calculated as follows:

$$420 \quad \text{Mean Bias (MB in DU)} = \frac{\sum_{i=1}^N y_{i(sat)} - y_{i(ref)}}{N}$$

421

$$422 \quad \text{Normalized Mean Bias (NMB in \%)} = \frac{1}{N} \sum_{i=1}^N \frac{y_{i(sat)} - y_{i(ref)}}{y_{i(ref)}} \times 100$$

423

424 N is the number of monthly TCO observations over a given region/site and y_i is the
 425 monthly mean TCO based on in situ data (ref) or satellite data (sat).

426 In order to represent the relationship between the satellite data and the in situ data, we
 427 used a least-square linear regression as well as the orthogonal distance regression (ODR). In this
 428 exercise, we are not using strict sampling criteria in time and space (except for the satellite and
 429 in-situ observations being in the same month, year and grid cell), nor smoothing in situ ozone
 430 profiles to the vertical resolution of the satellite data before integration. To extract satellite data
 431 over IAGOS and ATom regions, we used a 5°x5° gridded mask reflecting monthly grid cells with
 432 available IAGOS and ATom data, and only these grids are used to compute regional mean
 433 satellite values. For comparison to SHADOZ data, satellite data were extracted at the latitude and
 434 longitude of the SHADOZ sites (sonde launch site within satellite pixel). We include all satellite
 435 records with a minimum of one year of data within 2014-2019.

436

437 **2.5 Fused product and trend estimation**



438 The tropical region has sparse in situ sampling in both time and space, which makes
439 accurate quantification of trends challenging. Based on a sampling sensitivity test (section S1,
440 Figures S2 and S3), we conclude that one profile per week is only sufficient for detection of
441 trends with a very strong magnitude (i.e., $> |3| \text{ nmol mol}^{-1} \text{ decade}^{-1}$), which is not common in the
442 free troposphere. We show that a sampling frequency of 7 profiles per month is sufficient for
443 basic trend detection (i.e., to reliably determine if there is a trend) of TTO using the datasets
444 presently available (if the magnitude of a trend is greater than $|1| \text{ nmol mol}^{-1} \text{ decade}^{-1}$), but
445 additional data are required for accurate quantification or detection of a weaker trend.

446 Because the sparse sampling makes trend detection difficult, we have chosen to
447 statistically fuse the in situ measurements from the IAGOS and SHADOZ programs over large
448 regions, which includes air masses from different origins and influences (Figures 1 and S7 to
449 S11). The method is based on a data fusion technique described by Chang et al. (2022), which
450 considers ozone correlation structure, sampling frequency and inherent data uncertainty. By
451 investigating systematic ozone variability, the resulting fused product allows us to reconcile the
452 differences between heterogeneous datasets and enhance the detectability of trends. For the
453 Americas, we fused SHADOZ data over San Cristobal and Paramaribo with the IAGOS data
454 (Figure S7); for Southeast Asia, we fused SHADOZ over Hanoi with the IAGOS data (Figure
455 S8); for Malaysia/Indonesia, we fused SHADOZ data over Kuala Lumpur and Watukosek (Java)
456 with the IAGOS data (Figure S9). For Western Africa and India, SHADOZ data are not available
457 and we show the timeseries of just the IAGOS data in Figure S10 and S11, respectively.

458 For IAGOS data and the fused product, the trend estimate and its associated uncertainty
459 are based on quantile regression (Koenker & Hallock, 2001), which is an appropriate choice for
460 ozone profile time series, because of the irregular sampling schemes and the need to evaluate
461 ozone changes associated with a range of percentiles (Chang et al., 2021). Data gaps are not
462 interpolated as interpolation creates fictitious sample sizes for trend detection, while treating the
463 missing data as not substantially deviant from the available data variability. Due to limited
464 available sample sizes, only median trends (i.e., an estimate of the trend based on median data
465 values) are reported in this study. To account for potential correlation between ozone and climate
466 variability, such as ENSO (El Niño-Southern Oscillation) and QBO (quasi-biennial oscillation),
467 the trend model is specified through:

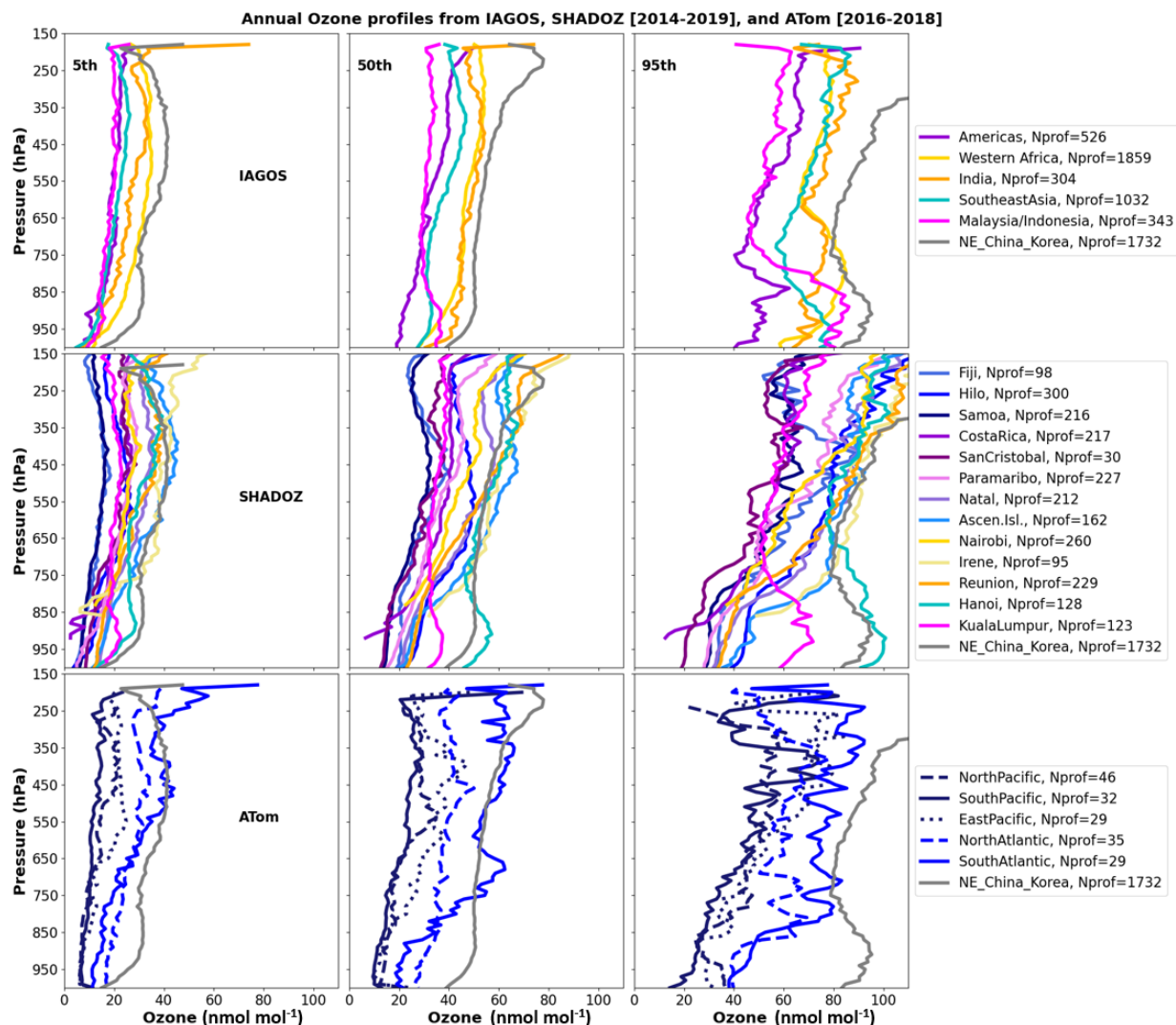
$$468 \text{anomaly} = b_0 + b_1 \text{Trend} + b_2 \text{ENSO} + b_3 \text{QBO}(30\text{mb}) + b_4 \text{QBO}(50\text{mb}) + \text{Noise} \quad [1]$$

470
471 where b_0 is the intercept, b_1 is the linear trend, b_2 is the regression coefficient for ENSO, b_3 and
472 b_4 are coefficients for QBO at 30 and 50 mb, respectively. The trend uncertainty is derived by a
473 bootstrapping method (Feng et al., 2011). The ENSO and QBO indexes can be found in the data
474 availability section. Figure S12 shows that if ENSO and QBO are not considered, the trends can
475 be offset by about $1\text{-}2 \text{ nmol mol}^{-1} \text{ decade}^{-1}$ at individual pressure layers over the five IAGOS
476 regions, except Africa where the trend differences are negligible.

477 In addition, we conducted trend analysis of the monthly TCO from SHADOZ, IAGOS,
478 OMI and OMI/MLS as well as the tropical ozone burden (TOB, Tg decade^{-1}) over zonal monthly
479 means using OMI and OMI/MLS. The OMI/MLS TCO has shown a drift over time that we
480 corrected for this study (see section S2).



481
 482 **3. Results**
 483 **3.1 Ozone Profiles**
 484



485
 486 **Figure 2.** Distribution of TTO showing annual 50th, 5th and 95th percentiles (left, center, and right
 487 columns, respectively) of ozone profiles (nmol mol^{-1}) measured by IAGOS (top), SHADOZ
 488 (middle) both between 2014 and 2019, and ATom (bottom) between 2016 and 2018. The colors
 489 correspond to the IAGOS, ATom regions and SHADOZ sites (see Figure 1). The North China
 490 and Korea (NE_China_Korea) region from IAGOS data is plotted in grey on all panels as a
 491 reference for mid-latitude polluted regions.
 492



493 For the period 2014–2019 (IAGOS, SHADOZ) and 2016–2018 (ATom), the three in situ data sets
494 show a range of ozone values from the surface to 200 hPa, indicative of the different
495 photochemical and transport regimes across the tropics (Figure 2). Here we highlight several
496 notable features. The 50th and 95th percentiles of SHADOZ data over Hanoi (up to 100 nmol mol⁻¹)
497 are much higher than at the other sites/regions, especially below 750 hPa. Hanoi experiences
498 strong regional ozone production with a significant contribution from biomass burning in the
499 Indochina peninsula, especially in spring (Ogino et al., 2022). Ozone is lowest above the tropical
500 South Pacific (dark blue lines on the SHADOZ and ATom panels of Figure 2) and the Americas
501 (purple lines on the IAGOS, SHADOZ panels of Figure 2) with the 5th percentile less than 10
502 nmol mol⁻¹, especially in the lower troposphere. The 95th percentile ozone is highest above
503 Africa, India and Southeast Asia in the mid- and upper troposphere, and above Southeast Asia
504 and Malaysia/Indonesia in the boundary layer. The tropical South Atlantic (ATom and
505 Ascension Island) is also notable due to broad enhancements from the lower free troposphere to
506 the upper troposphere, with values of 60–80 nmol mol⁻¹. Similar patterns are seen in the median
507 (50th percentile) ozone profiles, albeit with lower mixing ratios.

508 As a frame of reference, we show the polluted mid-latitude region of Northeast China /
509 Korea from IAGOS data in 2014–2019, notable for its high ozone values (Gaudel et al., 2020). In
510 most cases the ozone profiles of Northeast China / Korea are similar to the maximum tropical
511 ozone profiles, but some regions exceed the Northeast China / Korea ozone values, such as
512 Southeast Asia / Hanoi, Southern Africa, and the tropical South Atlantic / Ascension Island.

513 Based on observations from the 1980s and 1990s, ozone levels in the tropics have
514 generally been considered to be lower than in the mid- and high latitude regions, with the
515 exception of the tropical Atlantic (Logan et al., 1999; Fishman et al., 1990). However, with
516 greater availability of ozone profiles across the tropics we can now demonstrate that tropical
517 India, Southeast Asia, and Malaysia/Indonesia are among the most polluted regions and are
518 comparable to the mid-latitude regions in terms of ozone pollution (Figure 2). We note that this
519 unique finding regarding India only pertains to the tropical regions as ozone enhancements
520 across northern India were detected by the TOMS/SBUV instruments as far back as 1979
521 (Gaudel et al., 2018).

522

523 **3.2 Tropical Tropospheric Column Ozone (TTCO)**

524

525

526

527

528

529

530

531

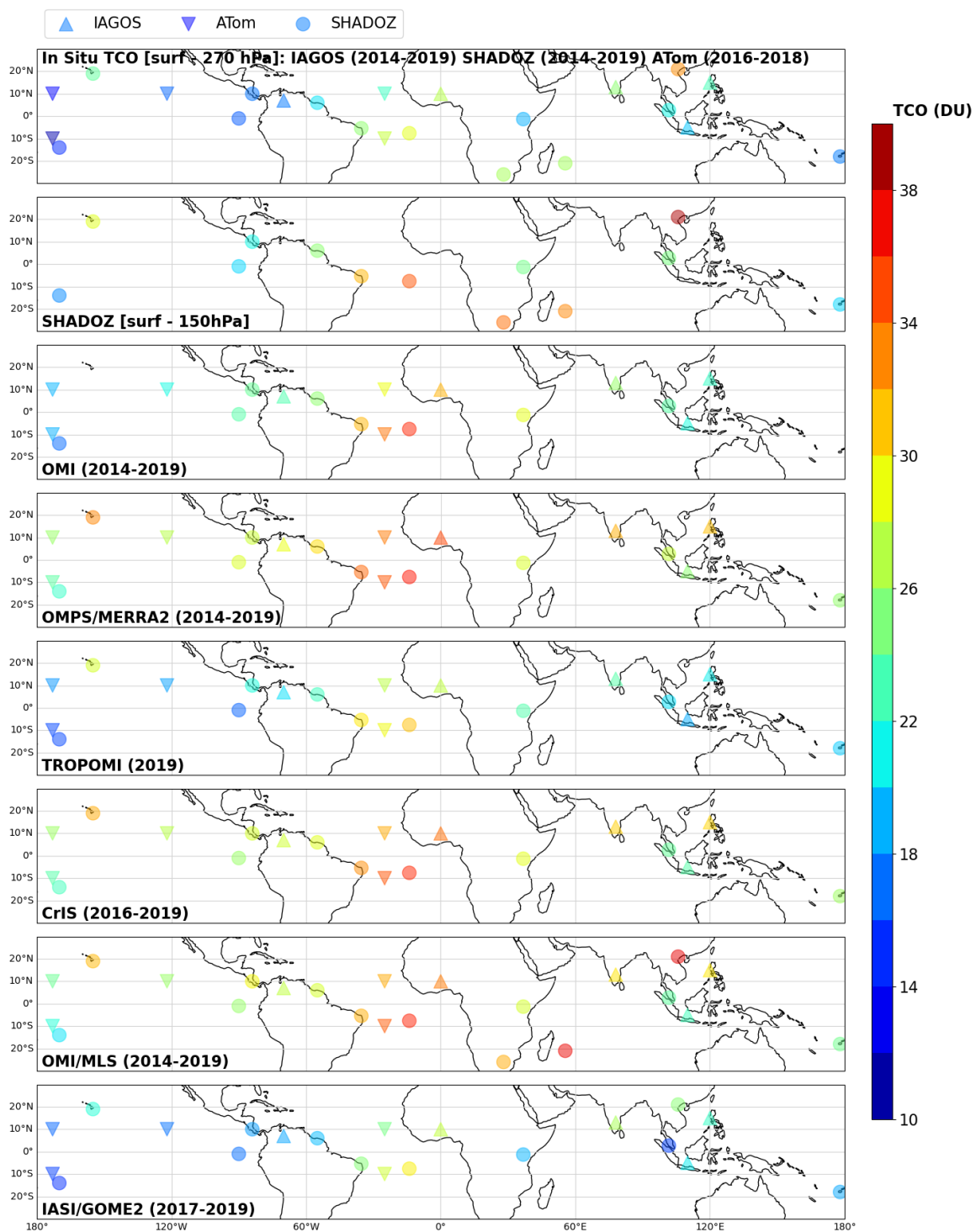
532

533

534

535

536





538

539 **Figure 3.** Annual tropical tropospheric column ozone (TTCO, surface-270 hPa) from in situ data
540 (IAGOS, SHADOZ between 2014 and 2019 and ATom between 2016 and 2018) (top panel),
541 TTCO (surface-150 hPa) from SHADOZ (2nd panel) between 2014 and 2019; and from OMI
542 (surface to 100 hPa, 2014-2019), OMPS/MERRA2 (surface to potential temperature at 380 K,
543 2014-2019), TROPOMI (surface to 270 hPa, 2019), CrIS (surface to 2016-2019), OMI/MLS
544 (surface to thermal tropopause, 2014-2019) and IASI/GOME2 (surface to 12 km, 2017-2019).

545

546



547 Figure 3 shows the tropical tropospheric column ozone (TTCO) for SHADOZ, IAGOS
548 and ATom and for the six-satellite records (OMI, OMPS/MERRA2, TROPOMI, CrIS,
549 OMI/MLS and IASI/GOME2). As mentioned in Section 2, we focus on the 2014-2019 time
550 period to study the TTCO distribution. However, ATom data are only available between 2016
551 and 2018, and some satellite records only cover one or two years within the five-year period we
552 have chosen. The in situ columns in Dobson units (DU) shown on the first panel of Figure 3 are
553 from the surface to 270 hPa, with ozone varying between 11 and 33 DU. When the TTCO is
554 calculated with profiles extending up to 150 hPa (2nd panel of Figure 3 with SHADOZ only),
555 ozone varies between 18 and 39 DU. As seen with the profiles (section 3.1), the minimum TTCO
556 values are observed over the Pacific Ocean and the maximum TTCO values are observed over
557 the Atlantic, Africa, India and Hanoi. The six-satellite records reproduce quite well the
558 variability of ozone with longitude. However, the range of TTCO values varies by product.
559 TTCO values under 20 DU are found over the Pacific Ocean with OMI CCD, TROPOMI and
560 IASI/GOME2, and over Southern Asia with IASI/GOME2. TTCO values above 30 DU are
561 found over the Atlantic Ocean with all satellite records except IASI/GOME2, and over Africa,
562 India and Southeast Asia with OMPS/MERRA2, CrIS and OMI/MLS.

563 Qualitatively, the mid- to upper tropospheric ozone maximum above the Atlantic and
564 Africa is well known (Fishman et al., 1987; Thompson et al., 2003) and explained by subsidence
565 of air masses rich in ozone (Krishnamurti et al., 1996; Thompson et al., 2000, 2003), emissions
566 of lightning NO_x (LiNO_x, Sauvage et al., 2007), emissions of CO/VOCs from biomass burning
567 (Ziemke et al., 2009; Bourgeois et al., 2021) and urban emissions (Tsivlidou et al., 2022). Hanoi,
568 at the northern edge of our domain, shows previously documented large ozone enhancements
569 (Ogino et al., 2022), equivalent to those above Africa and the Atlantic. A new maximum,
570 equivalent to that found above Africa, is now detected over India, mostly related to human
571 activities (fossil fuel combustion and agriculture burning) (Singh et al., 2020).

572 However, the accurate quantification of TTCO remains a challenge. The following
573 section quantifies the differences between the satellite and in situ data in order to improve the
574 accuracy of TTCO estimates from space.

575

576 **3.3 How do the current tropospheric ozone satellite records perform?**

577

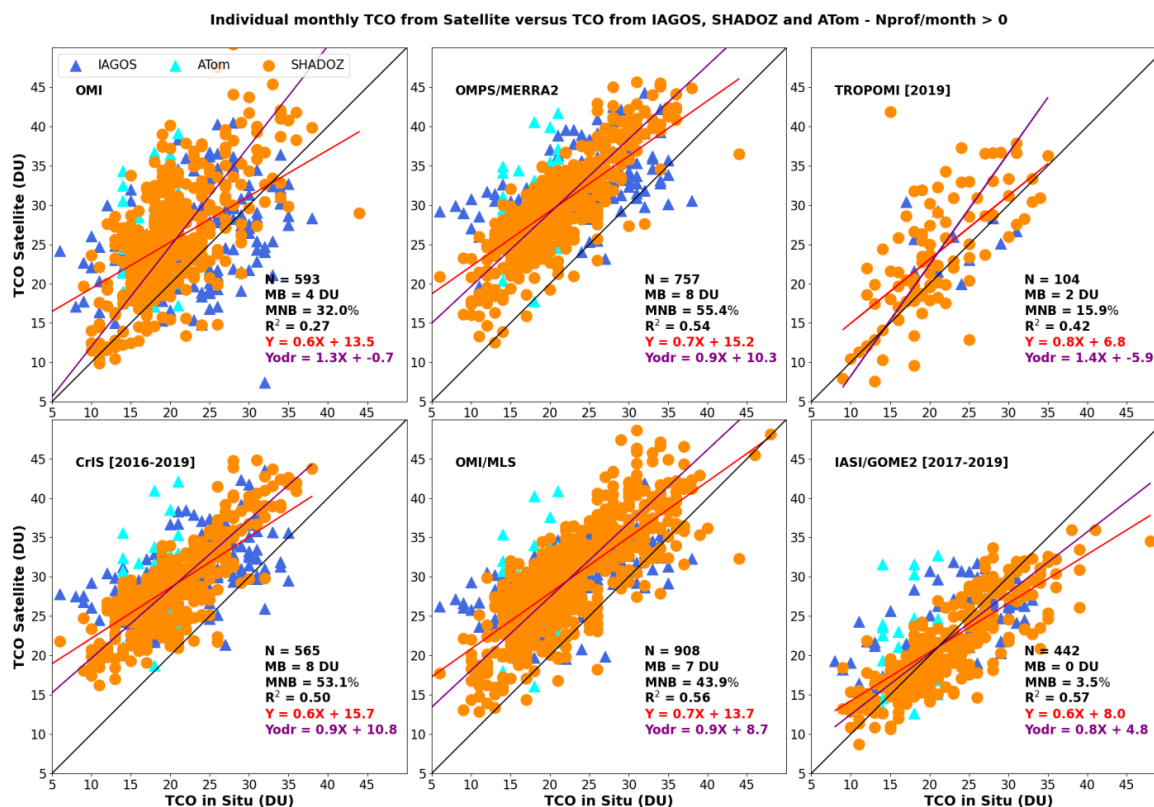
578

579

580

581

582



583

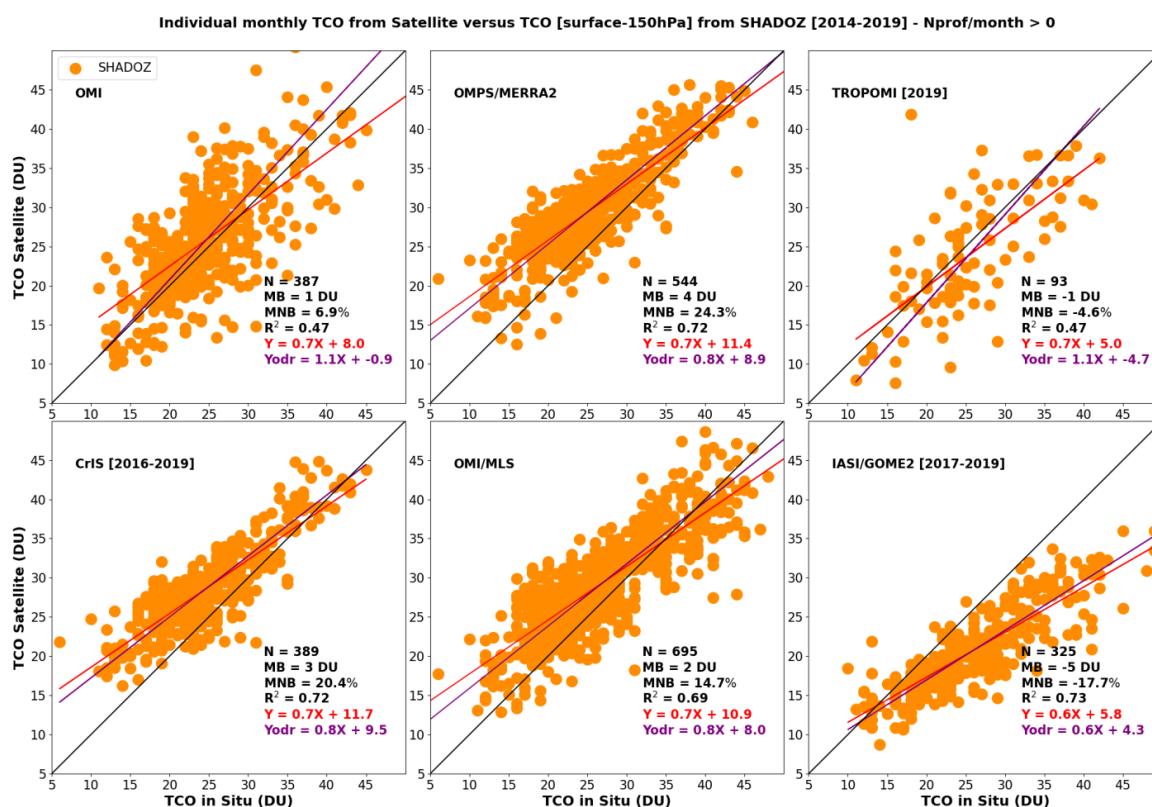
584

585 **Figure 4.** Scatter plot of the monthly TTCO from OMI, OMPS/MERRA2, TROPOMI, CrIS,
 586 OMI/MLS and IASI/GOME2 satellite records compared with the in situ TTCO from IAGOS
 587 (dark blue triangles), ATom (cyan triangles) and SHADOZ (orange circles) between 2014 and
 588 2019. The in situ TTCO values are calculated between the surface and 270 hPa. The TTCO for
 589 all satellite data extends much higher (typically up to 100-150 hPa), except for TROPOMI
 590 (TTCO calculated from the surface up to 270 hPa) and IASI/GOME2 (TTCO up to 12 km/200
 591 hPa) (Figure S1). The linear least-squares regression is shown in red. The linear orthogonal
 592 distance regression is indicated in purple. The number of points (N), the mean biases (MB), the
 593 mean normalized biases (MNB) and the correlation coefficient (R²) are shown in black. N
 594 corresponds to the number of months with both in situ and satellite data multiplied by the
 595 number of IAGOS regions, ATom regions and SHADOZ sites over the time period 2014-2019.
 596

597 The overall satellite biases of TTCO against in situ TTCO from IAGOS, ATom and
 598 SHADOZ are shown in Figure 4. All satellite TTCO values tend to bias high, with mean
 599 differences varying from 0 DU to 9 DU. The positive bias is expected since the top level of the
 600 satellite TTCO lies higher than that of the in situ data, except for TROPOMI and IASI/GOME2.
 601 Figure 4 shows a mean TTCO bias of 2 DU for TROPOMI and no TTCO bias for IASI/GOME2.



602 For TROPOMI and IASI/GOME2, showing the lowest TTCO biases, the sign of the differences
 603 can change with location (Figure S13). TROPOMI shows positive TTCO biases of 1-4 DU from
 604 the Pacific to Africa and negative biases of 1-2 DU above India, Indonesia/Malaysia.
 605 IASI/GOME2 also shows negative TTCO biases of 1-5 DU above India and Indonesia/Malaysia.
 606 When using only SHADOZ data, rather than all three in situ data sets, as a reference for the
 607 TTCO from the surface to 270 hPa (Figure S14), the mean biases remain the same (compared to
 608 Figure 4), whereas the correlation coefficient and the mean normalized biases increase.
 609



610

611

612 **Figure 5.** Same as Figure 4 but for satellite data compared with SHADOZ TTCO integrated

613 between the surface and 150 hPa.

614

615 Because four satellite records (OMI, OMPS/MERRA2, CrIS and OMI/MLS) show
 616 TTCO from the surface to 100-150 hPa, altitudes that the IAGOS aircraft do not reach, we
 617 compare them to SHADOZ TTCO from the surface to 150 hPa (Figure 5). Both the biases and
 618 the correlation coefficients improve when compared to results for TTCO up to 270 hPa, except
 619 for IASI/GOME2 for which the bias became negative (-5 DU). These results illustrate that
 620 differences in the definition of the top level of the tropospheric column play an important role in



621 observed differences between satellite TCO and in-situ TCO ozone data. There is hence a
622 need for a common tropospheric column definition to make satellite TCO estimates comparable
623 between each other and with in-situ data.

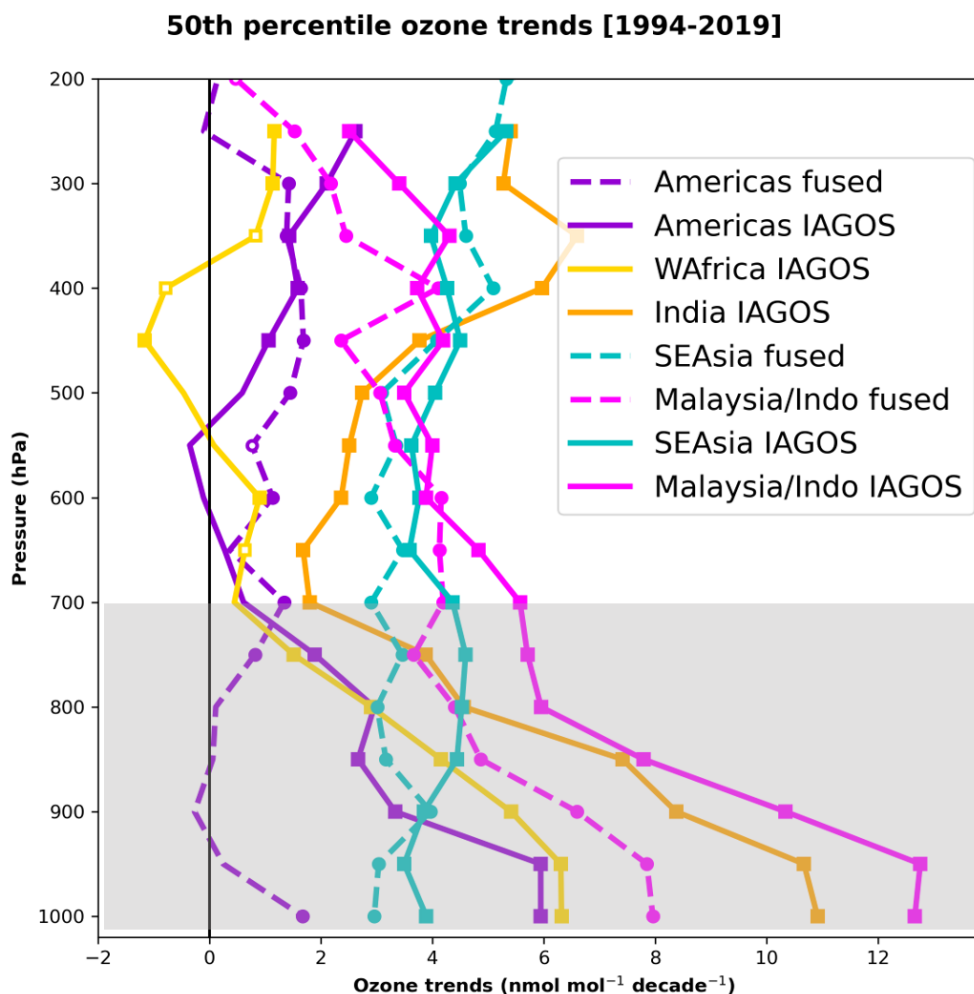
624 Looking at the SHADOZ sites individually (Figure S15), the biases became closer to zero
625 above Ascension Island (tropical Atlantic) and Natal (Brazil) when the top level of the column
626 was changed from 270 hPa to 150 hPa. However, the satellite TCO records with the top level of
627 the column higher than 270 hPa (all satellites except TROPOMI and IASI/GOME2) still
628 overestimate TCO after changing the reference SHADOZ TCO's top level from 270 hPa to
629 150 hPa.

630 The biases of TROPOMI reported in Figures 4, S11 and 5 are in the range of those
631 reported in Hubert et al. (2021) with a bias of 2.3 ± 1.9 DU when compared with the SHADOZ
632 ozonesondes. Biases estimated for TROPOMI and IASI/GOME 2 using the three in situ TCO
633 data sets from the surface to 270 hPa (Figure 4), and biases estimated for OMI,
634 OMPS/MERRA2, CrIS and OMI/MLS using SHADOZ TCO from the surface to 150 hPa
635 (Figure 5) are applied to improve the accuracy of estimates of the tropospheric ozone burden
636 (TOB), as described in section 3.5.

637

638 **3.4 Ozone changes with time**

639

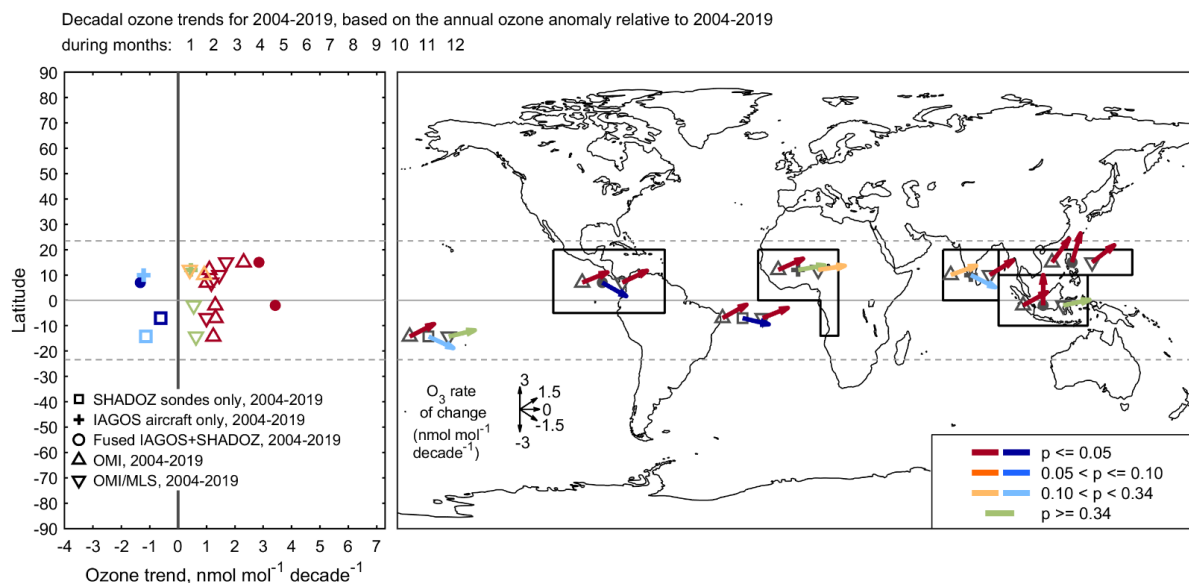


640
 641 **Figure 6.** Vertical profiles of ozone trends ($\text{nmol mol}^{-1} \text{ decade}^{-1}$) between 1994 and 2019, at 50
 642 hPa vertical resolution. Trends are calculated for the 5 IAGOS regions in the tropics:
 643 Americas, Western Africa, India, Southeast Asia and Malaysia/Indonesia. SHADOZ data are
 644 available for 3 out of the 5 IAGOS regions and used to produce fused trends (IAGOS +
 645 SHADOZ). Filled squares (IAGOS trends) or circles (fused trends) indicate trends with p -values
 646 less than 0.05. Open squares or circles indicate trends with p -values between 0.05 and 0.1. The
 647 zero-trend value is indicated with a vertical black line. The vertical range below 700 hPa is
 648 shaded grey to indicate that the fused trends are based on several sites and airports influenced by
 649 different local air masses. The 2-sigma values associated with the ozone trends are shown in
 650 Figure S16.
 651



652 The estimation of trends of tropospheric ozone in the tropics based on in situ observations
653 is a difficult task as the data are sparse in time and space, as discussed below. In this study, the
654 Americas, Africa, Southeast Asia and Malaysia/Indonesia are regions sampled both by IAGOS
655 and SHADOZ allowing us to improve the trends estimate in the free troposphere (above 700
656 hPa) by fusing both datasets to achieve a greater sample size and a better representation of
657 regional ozone variability (sections 2.5, S1 and Figures S2-S8). Figure 6 shows trends from the
658 fused datasets and also from the IAGOS data only. We observed increasing ozone levels between
659 1994 and 2019 over Americas (trends ranging from -0.3 ± 0.6 to 1.8 ± 0.7 nmol mol⁻¹ decade⁻¹
660 with the vertical levels), Africa (from -0.3 ± 0.6 to 7.4 ± 0.4 nmol mol⁻¹ decade⁻¹), India (from
661 0.9 ± 1.4 to 11 ± 2.4 nmol mol⁻¹ decade⁻¹), Southeast Asia (from 2.5 ± 0.4 to 5.1 ± 0.8 nmol mol⁻¹
662 decade⁻¹) and Malaysia/Indonesia (from 0.5 ± 0.6 to 8.0 ± 0.8 nmol mol⁻¹ decade⁻¹). In the
663 boundary layer (<700 hPa), local air masses sampled above SHADOZ sites and IAGOS airports
664 are likely very different in terms of emissions, photochemistry and air mass history, which may
665 explain higher differences between the fused and IAGOS trends than in the free troposphere. The
666 strongest trend we find is 12.5 ± 2.2 nmol mol⁻¹ decade⁻¹ in the boundary layer over
667 Malaysia/Indonesia using IAGOS data only. Malaysia/Indonesia is the region for which the
668 number of years with missing data is excessive. However, we do not expect this gap to alter the
669 trend's estimate because, as mentioned in the Methods section and based on Blot et al. (2020),
670 MOZAIC and IAGOS data sets are consistent, and together they yield continuous multi-decadal
671 data records. As shown by Gaudel et al. (2020), the “L” shape of the trends, with a rather
672 constant trend above the 700 hPa level and larger trends in the boundary layer, is common to the
673 studied tropical regions except for Southeast Asia, which shows similar trends in both the
674 boundary layer and in the free troposphere. Taking the fused trends as the reference, we find that
675 the trends estimated using IAGOS data only tend to be overestimated by 1-2 nmol mol⁻¹ decade⁻¹
676 at 700-500 hPa, except over the Americas, and underestimated by 0.5-1 nmol mol⁻¹ decade⁻¹ at
677 500-250 hPa, except over Malaysia/Indonesia. Only IAGOS ozone profiles are available over
678 India and the trends in this region can reach up to 6.7 ± 1.8 nmol mol⁻¹ decade⁻¹ at 350 hPa,
679 which exceed the trends over the other regions at the same vertical level.

680
681
682
683



684

685 **Figure 7.** TTCO trends ($\text{nmol mol}^{-1} \text{decade}^{-1}$) between 2004 and 2019 from IAGOS (crosses),
 686 SHADOZ (squares), IAGOS fused with SHADOZ (circles), OMI (triangles up) and OMI/MLS
 687 (triangles down) above the five continental IAGOS regions (Americas, Africa, India, Southeast
 688 Asia and Malaysia/Indonesia) and two oceanic SHADOZ regions (Samoa and Natal + Ascension
 689 Island). The left panel shows the trends of ozone as a function of latitude. The right panel shows
 690 the trends of ozone on the map with the black rectangles demarcating the five IAGOS regions.
 691 On the map, the longitude of the crosses, circles, triangles and squares are arbitrary and the
 692 latitude is the mean latitude of the black rectangles or relative to the SHADOZ sites. The
 693 direction of the arrows shows the magnitude of the trends and the colors indicate the p -value.
 694 The TTCO trends from in situ data are calculated from the monthly TTCO between the surface
 695 and 100 hPa, except over India where IAGOS profiles are available between the surface and
 696 around 200 hPa. The TTCO trends from OMI and OMI/MLS are calculated from the monthly
 697 TTCO defined between the surface and around 102-105 hPa (Figure S1).

698

699 Satellite data from OMI are available continuously since 2004 and 15-year trends cannot
 700 be estimated. The interannual variability of the TTCO from satellite and in situ data is shown in
 701 Figure S17. Several time series of the monthly mean of tropospheric ozone above
 702 Malaysia/Indonesia show the influence of climate variability such as El Niño and related fires.
 703 For example, we see a peak of ozone in September 2015 in agreement with a peak of CO
 704 emissions due to biomass burning above Equatorial Asia (Figure S18, Mead et al., 2018).

705 Figure 7 and Table 1 show the trend estimates of TTCO in $\text{nmol mol}^{-1} \text{decade}^{-1}$ from
 706 OMI CCD, OMI/MLS, and in situ data between 2004 and 2019. The in situ trends between 2004
 707 and 2019 (Figure S19 and Table 1) are negative for Samoa ($-1.1 \pm 1.9 \text{ nmol mol}^{-1} \text{decade}^{-1}$),
 708 Americas ($-1.3 \pm 0.4 \text{ nmol mol}^{-1} \text{decade}^{-1}$), Natal/Ascension Island ($-0.6 \pm 0.5 \text{ nmol mol}^{-1}$



709 decade⁻¹) and India (-1.2 ± 1.8 nmol mol⁻¹ decade⁻¹), and positive for Western Africa (0.4 ± 1
710 nmol mol⁻¹ decade⁻¹), Southeast Asia (2.9 ± 1.4 nmol mol⁻¹ decade⁻¹) and Malaysia/Indonesia
711 (3.4 ± 1.3 nmol mol⁻¹ decade⁻¹). The presence of negative trends above some regions for the
712 shorter 2004–2019 period differs greatly from the longer 1994–2019 time period which had no
713 time series with negative trends except above Samoa (Figure 7, Table 1). They also differ from
714 the positive trends shown by the satellite data (full record, Figure 7, Table 1). The satellite trends
715 vary between 0.9 ± 1.3 nmol mol⁻¹ decade⁻¹ over India and 2.3 ± 1.3 nmol mol⁻¹ decade⁻¹ over
716 Southeast Asia with OMI, and between 0.4 ± 0.8 nmol mol⁻¹ decade⁻¹ over Western Africa and
717 1.7 ± 0.8 nmol mol⁻¹ decade⁻¹ over Southeast Asia with OMI/MLS (Figure 7, Table 1).

718 Discrepancies between satellites and in situ observations in assessing trends may be
719 caused by (i) the different definitions of the tropospheric column (100 hPa, 200 hPa or
720 tropopause defined with the temperature lapse rate); (ii) the diminished sensitivity of the space-
721 based instruments in the boundary layer; or (iii) the limited data availability and relatively short
722 record that may lead to less accurate and precise trends (Figures S2 and S3). In particular we
723 highlight previous research that has demonstrated the difficulty in detecting ozone trends in time
724 series that are noisy and or sparsely sampled (Weatherhead et al., 1998; Fischer et al., 2011;
725 Barnes and Fiore, 2016; Fiore et al., 2022). These studies show that 20 years of observations, or
726 more, are needed for trend detection, and that model ensembles (based on differing initial
727 conditions) can produce trends for a given location that vary so widely that even the sign can
728 fluctuate between positive and negative, when dealing with time periods less than 20 years.
729 Furthermore, previous studies of in situ ozone profiles concluded that a sampling frequency of
730 once per week generally fails to produce accurate monthly mean and trend values (Logan, 1999;
731 Saunio et al., 2012; Chang et al., 2020, 2022). Consistent with these previous studies, we
732 conducted our own analysis of tropical ozone time series (see the Supplementary Section S1) and
733 found that these sparsely sampled data sets have very low signal-to-noise ratios, which makes
734 trend detection very difficult, especially when a time series is less than 20 years in length (Chang
735 et al., 2020, 2022). The comparison between the in situ and satellite trends is only 15 years in
736 length (2004–2019), and the in situ datasets are sparsely sampled, characteristics consistent with
737 known challenges for trend detection. Furthermore, we point out that the robustness of the
738 positive trends from the satellite records greatly diminishes, and even becomes undetectable,
739 when we reduce the sample size of the satellite data in the IAGOS regions to match the sparse
740 sampling frequency of the aircraft observations (Figure S20). For example, when the satellite
741 data are fully sampled across the five IAGOS domains, all trends are positive, within the range
742 0.4 ± 0.8 to 2.3 ± 1.3 nmol mol⁻¹ decade⁻¹. But when the satellite sample sizes are reduced so
743 that they only coincide with the specific months and grid-cells sampled by the IAGOS aircraft,
744 the range of the trends more than doubles and even includes negative values (-3.1 ± 2.6 to $+3.6 \pm$
745 2.1 nmol mol⁻¹ decade⁻¹). This increased uncertainty is an expected outcome of decreased
746 sampling frequency, as illustrated in Figure S2.

747 The color scheme in Table 1 reflects our overall confidence in the presence of in situ
748 trend estimates, according to the number of missing monthly values, monthly average data
749 availability, the length of study period, and the *p*-value of the trend estimate (the trends are
750 confident only if a low *p*-value and a high data coverage are met, see Appendix A for further
751 details and Section S3 for a discussion of the confidence assigned to each region). When
752 assigning a level of confidence to a trend we weigh the *p*-value and the data coverage and ask the
753 question: “Are we confident that a positive or negative trend is reliable?” For example, if a
754 positive trend has a low *p*-value but also low data coverage then our confidence that the trend is



755 reliable is diminished. Western Africa is the only region in this study with sufficient sampling
756 for reliable trend detection with high confidence (1994-2019). Trends derived from the other in
757 situ time series only have low or medium confidence due to sampling deficiencies and/or low
758 estimation certainty (based on the p-value). When we compare the satellite trends to the in situ
759 trends we find that they are consistent for Southeast Asia, with all three data sets showing
760 positive trends. In the other regions we find discrepancies between the in situ and satellite trends,
761 but in these regions, we do not have high confidence in the in situ trends, and therefore there is
762 no reason to reject the satellite trend values, which generally indicate an increase of ozone in the
763 study regions. However, the discrepancies between satellite and in situ trends in the Americas
764 and Natal + Ascension Island are nuanced and require further discussion. In the Americas region
765 we assigned medium confidence to the decreasing ozone trends based on the in situ observations,
766 which contrasts strongly with the clear positive trends based on the satellite data. When we
767 reduced the satellite sampling coverage to match the locations and months with IAGOS
768 observations, we found that the satellite trends switched from clear positive trends to clear
769 negative trends (Figure S20). This exercise indicates that the available in situ observations are
770 not representative of the large region, and therefore they do not provide sufficient justification
771 for rejecting the positive trends reported by the satellite data. In situ ozone trends above Natal +
772 Ascension Island have a weak negative trend ($-0.62 \pm 0.54 \text{ nmol mol}^{-1} \text{ decade}^{-1}$) with medium
773 confidence, while the satellite trends show weak positive trends. While the divergence between
774 the positive and negative trends is small over this short time period (2-3 nmol mol^{-1} over 15
775 years), this discrepancy warrants further investigation to determine the differences between the
776 satellite and in situ time series trends.

777

778 **3.5 Comparison to previous studies**

779 Using the ozonesondes from the SHADOZ network, Thompson et al. (2021) found
780 positive annual trends of about $1.2 \pm 3 \text{ \% decade}^{-1}$ to $1.9 \pm 3 \text{ \% decade}^{-1}$ ($0.08 \pm 1.68 \text{ nmol mol}^{-1}$
781 decade^{-1} to $0.78 \pm 1.66 \text{ nmol mol}^{-1} \text{ decade}^{-1}$) between 1998 and 2019 at 5-10 km (~500-250 hPa)
782 across the tropical belt. They reported maximum trends ($1.9 \pm 3 \text{ \% decade}^{-1}$) above the
783 Malaysia/Indonesia (Kuala Lumpur + Java) and Americas (San Cristobal + Paramaribo) regions
784 and minimum trends ($1.2 \pm 3 \text{ \% decade}^{-1}$) above Africa (Nairobi). The SHADOZ trends are
785 slightly lower than the IAGOS + SHADOZ fused trends or IAGOS trends which may be
786 explained by the different starting points of the time series (1998 for SHADOZ data and 1994 for
787 IAGOS data), but they are all positive.

788 Previous studies of TCO trends from satellite data relied on data harmonization in order
789 to combine several satellite records into a time series spanning at least two decades and to better
790 account for the climate variability in the trend estimates (Heue et al., 2016; Leventidou et al.,
791 2018; Ziemke et al., 2019; Pope et al., 2023). Heue et al. (2016) found a tropical trend of $0.7 \pm$
792 $0.12 \text{ DU decade}^{-1}$, with regional trends ranging from $+1.8 \text{ DU decade}^{-1}$ on the African Atlantic
793 coast, to $-0.8 \text{ DU decade}^{-1}$ over the western Pacific Ocean. Leventidou et al. (2018) reported
794 positive trends of TCO of 1 to $1.5 \text{ DU decade}^{-1}$ between 1996 and 2015 over Northern South
795 America, North Africa, South Africa and India, and negative trends of -1.2 to $-1.9 \text{ DU decade}^{-1}$
796 above the oceans (Pacific, Atlantic, Indian oceans). Using TOMS-OMI/MLS, Ziemke et al.
797 (2019) reported positive trends between 1979 and 2016 across the tropical latitude band 20°S -
798 20°N except above the southeastern tropical Pacific Ocean and southeastern Indian Ocean. The
799 highest positive trends (up to $1.3 \text{ DU decade}^{-1}$) were found above South-Southeast Asia and
800 Central Africa. Finally, a new harmonized product that quantifies ozone between the surface and



801 450 hPa reports much higher tropical trends than the other studies, with increases of 2.9 ± 1.6
802 DU decade⁻¹ for the southern tropical band (0 – 15° S) and 3.9 ± 1.8 DU decade⁻¹ for the northern
803 tropical band (0 – 15° N) for the years 1996-2017 (Pope et al., 2023). While these findings vary
804 regarding the magnitude of trends in the tropics, when taken into consideration with the 1994-
805 2019 in situ trends reported by the present study, the preponderance of evidence indicates a
806 general increase of TTCO since the mid-1990s.

807 Wang et al. (2022) report an increase of TTCO (950 - 250 hPa) trends using the GEOS-
808 Chem chemical transport model above the IAGOS' regions and SHADOZ sites between 1995
809 and 2017, except above Samoa. The trends vary with locations between -0.60 ± 0.38 nmol mol⁻¹
810 decade⁻¹ above Samoa and 2.87 ± 0.23 nmol mol⁻¹ decade⁻¹. In general, they find that the TTCO
811 trends from the model are lower by 1-3 nmol mol⁻¹ decade⁻¹ than from the observations, except
812 above Paramaribo.

813

814



815 **Table 1. Summary of the TCO trends in nmol mol⁻¹ decade⁻¹ from IAGOS, SHADOZ,**
 816 **OMI/MLS and OMI CCD.**

817 The sampling column reports three numbers for the in situ data: i) the number on the top refers to
 818 the average number of profiles per months taking into account all the months with profiles, ii)
 819 the number in the middle refers to the percentage of months with data for the studied time-period
 820 (1994-2019 or 2004-2019), iii) the number in the bottom refers to the total number of profiles for
 821 the studied time period (1994-2019 or 2004-2019). For the satellites, the sampling column
 822 reports “Full” when the full record is taken into account and “Filtered” when the satellite sample
 823 sizes have been greatly reduced so that they only coincide with the specific months and grid-cells
 824 sampled by the IAGOS aircraft. The table cells are color coded to reflect the low confidence
 825 (light blue), medium confidence (blue) and high confidence (dark blue) on the ozone trends from
 826 the in situ data based on the sampling and the p-value.

		1994-2019			2004-2019		
		Trends±2σ (nmol mol ⁻¹ decade ⁻¹)	p-value	Sampling	Trends±2σ (nmol mol ⁻¹ decade ⁻¹)	p-value	Sampling
IAGOS	Western Africa	2.34±0.48	<0.01	18.8 71.8% 3411	0.44±1.04	0.40	20.2 66.7% 2261
	India	5.68±1.06	<0.01	7.6 66.7% 1574	-1.21±1.76	0.17	8.5 67.7% 1100
SHADOZ	Samoa	-0.03±1.21	0.97	3.2 92.8% 779	-1.13±1.90	0.23	3.1 91.6% 537
	Natal + Ascension Island	0.49±0.49	0.04	6.3 90.4% 1426	-0.62±0.54	0.01	6.0 87.2% 939
Fused IAGOS + SHADOZ	Americas	0.47±0.79	0.36	12.2 92.2% 3642	-1.33±0.39	<0.01	10.7 93.6% 2036
	Southeast Asia	3.51±0.78	<0.01	11.2 77.8% 2501	2.85±1.38	<0.01	10.2 82.8% 1730
	Malaysia/Indonesia	3.96±0.53	<0.01	5.0 89.8% 1445	3.42±1.35	<0.01	4.7 89.9% 954
OMI CCD	Americas				1.01±0.72	0.01	Full
					-3.06±2.65	0.02	Filtered
	Western Africa				1.10±1.04	0.04	Full
					-1.04±3.08	0.50	Filtered
	India				0.92±1.26	0.15	Full
					1.20±2.95	0.42	Filtered
	Southeast Asia				2.31±1.34	<0.01	Full
					3.56±2.08	<0.01	Filtered
Malaysia/Indonesia				1.31±1.15	0.02	Full	
				2.26±3.42	0.19	Filtered	
Samoa				1.24±1.17	0.04		
				1.32±1.04	0.01		
OMI/MLS	Americas				1.17±0.72	<0.01	Full



					-2.79 ± 1.96	0.01	Filtered
Western Africa					0.41 ± 0.80	0.30	Full
					0.68 ± 3.95	0.73	Filtered
					1.45 ± 0.79	<0.01	Full
India					-1.64 ± 1.67	0.05	Filtered
					1.69 ± 0.83	<0.01	Full
Southeast Asia					2.46 ± 1.85	0.01	Filtered
					0.55 ± 1.22	0.37	Full
Malaysia/Indonesia					1.39 ± 4.36	0.53	Filtered
					0.63 ± 1.34	0.35	
Samoa					1.00 ± 0.78	0.01	
Natal + Ascension Island							

827

828

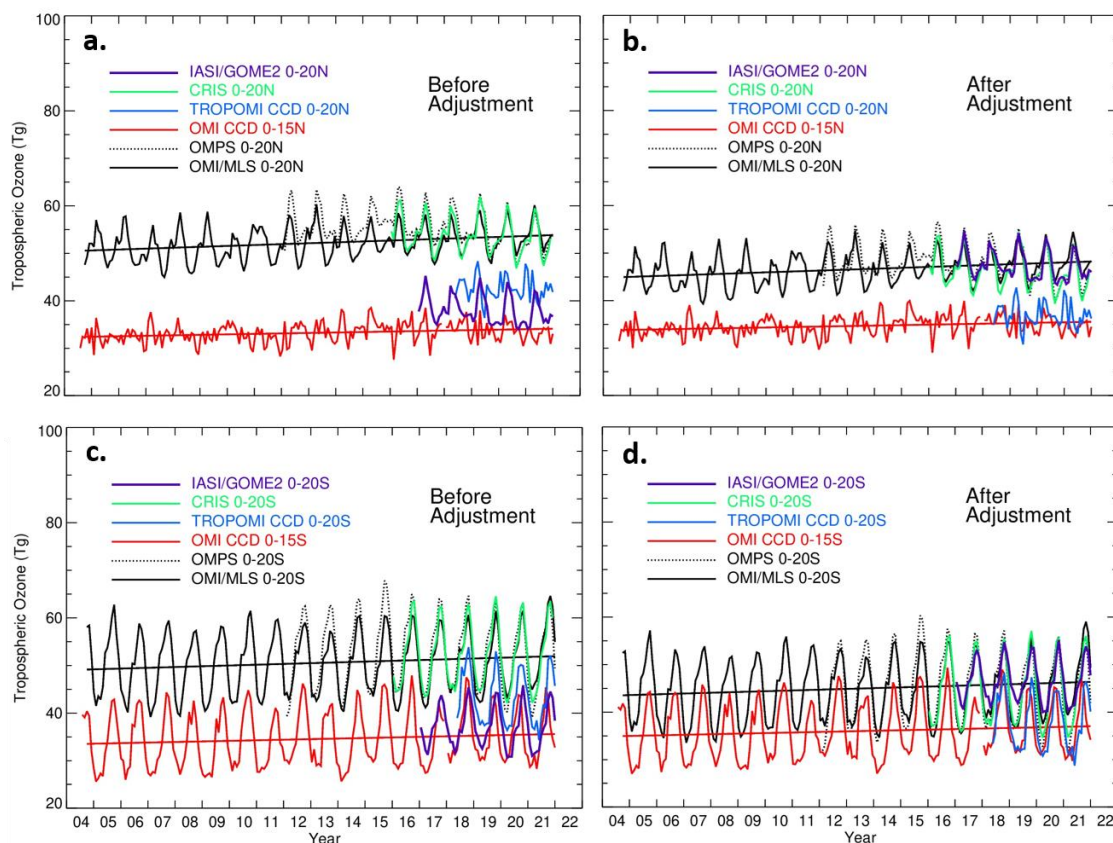
829

830



831 **3.6 Tropical tropospheric ozone burden**

832



833

834 **Figure 8.** Time series of tropospheric ozone burden (Tg) from OMI/MLS, OMPS/MERR2, OMI
835 CCD, TROPOMI, CrIS and IASI/GOME2. The panels show the monthly means for the Northern
836 Hemisphere (a and b) and the Southern Hemisphere (c and d) before and after bias correction.

837 The biases we used are in DU and from the differences between IASI/GOME2 and TROPOMI
838 TTCO using the reference TTCO up to 270 hPa and between OMI, OMI/MLS,
839 OMPS/MERRA2, CrIS TTCO using the reference TTCO up to 150 hPa (Figures 4 and 5).

840

841

842 Figure 8 shows the time series of the tropical tropospheric ozone burden (TTOB, Tg)

843 from six satellite records. As described in the Methods, OMI/MLS, OMPS/MERRA2,

844 TROPOMI, CrIS, and IASI/GOME2 are sampled in the 20°S-20°N latitude band, while OMI is

845 constrained to the 15°S-15°N latitude band. For both hemispheres we find two distinguished

846 groups in terms of TTOB (Figure 8, panels a and c): (i) OMI CCD, TROPOMI and

847 IASI/GOME2 with a range of TTOB of 25-45 Tg, (ii) OMI/MLS, OMPS/MERRA2 and CrIS

848 with a range of TTOB of 40-65 Tg. These differences are explained by the difference of latitude

849 coverage (OMI CCD) and the upper bound of the tropospheric column (lower for TROPOMI and



850 IASI/GOME2 than for the other satellite data). The seasonal variability of TTOB is lower in the
851 northern hemisphere than in the southern hemisphere especially in the narrowest latitude band
852 (OMI CCD).

853 The biases calculated from the scatter plots of satellite versus ozonesondes (Figures 4 and
854 5) are used to correct the satellite time series. The adjustment reduced the differences by about
855 10 Tg in the northern hemisphere and by 5 Tg in the southern hemisphere, between the two
856 groups mentioned above. In the northern hemisphere, after adjustment (Figure 8, panels b and d,
857 and Table 2), IASI/GOME TTOB (45-55 Tg) become part of group ii) and TROPOMI TTOB
858 (30-43 Tg) moved closer to OMI CCD TTOB in group i). In the southern hemisphere, it is
859 difficult to distinguish the two groups, after adjustment. For example, the range of
860 OMPS/MERRA2 TTOB (30-60 Tg) covers the range of the TTOBs in both groups after 2019.

861 Table 2 summarizes TTOB trends from this study, and from TOAR-Climate (Gaudel et
862 al., 2018). Trends are positive and higher in the northern hemisphere (1.4 ± 0.7 Tg decade⁻¹ to
863 5.7 ± 2.5 Tg decade⁻¹) than the southern hemisphere (0.9 ± 2.2 Tg decade⁻¹ to 5.1 ± 4.5 Tg
864 decade⁻¹). Because TTOB trends in Tg decade⁻¹ can increase with the width of the latitude band
865 (assuming trends are all positive across the range of latitudes considered), we also report trends
866 in % decade⁻¹, to compare trends between different latitude bands. We found that trends in the 0-
867 15° (OMI CCD) north and south latitude bands are lower than in the 0-20° (OMI/MLS) latitude
868 bands by 2-4 % decade⁻¹. These differences might be explained by a quicker increase of
869 tropospheric ozone in the subtropics than the equatorial region, or by a potential discrepancy
870 between OMI CCD and OMI/MLS. It is worth noting that the 2004-2016 OMI/MLS trends in the
871 0-30° north and south latitude bands are higher by a factor of 3 or 5 than the 2004-2019
872 OMI/MLS trends in the 0-20° north and south latitude bands. These differences might also be
873 explained by the influence of the larger increases of subtropical tropospheric ozone.

874

875



876 **Table 2.** Summary of tropical tropospheric ozone burden values and trends.

877

	Latitude band	Tropospheric Ozone Burden			Trends			
		Period	Instrument/ model	Values Tg	Period	Instrument	Values Tg/decade	Values %/decade
This study (These numbers are corrected using bias results from Figure 5)	0-15°N	2004-2019	OMI	31.8 ± 4.3	2004-2019	OMI	1.4 ± 0.7	4 ± 2
	0-15°S	2004-2019	OMI	32.9 ± 11.7	2004-2019	OMI	0.9 ± 2.0	2 ± 6
	0-20°N	2004-2021	OMI/MLS	46.6 ± 7.0	2004-2019	OMI/MLS	1.6 ± 1.1	3 ± 2
		2012-2021	OMPS	48.1 ± 7.4				
		2016-2021	CrIS	46.4 ± 7.5				
2017-2021		IASI/GOME 2	38.1 ± 5.9					
2019	TROPOMI	34.9 ± 5.1						
0-20°S	2004-2021	OMI/MLS	44.9 ± 13.0	2004-2019	OMI/MLS	0.9 ± 2.2	2 ± 5	
	2012-2021	OMPS	45.3 ± 15.1					
	2016-2021	CrIS	44.6 ± 13.4					
	2017-2021	IASI/GOME 2	37.1 ± 8.6					
	2019	TROPOMI	34.7 ± 10.7					
TOAR-Climate (Figures S28, S29)	0-30°N				2004-2016	OMI/MLS	5.7 ± 2.5	7 ± 3
	0-30°S				2004-2016	OMI/MLS	5.1 ± 4.5	6 ± 5.6

878

879

880



881 4. Conclusions

882 Long and mid-term records of tropospheric ozone from IAGOS, SHADOZ, and OMI, as
883 well as new observations from the ATom aircraft campaign and the CrIS, IASI/GOME2 satellite
884 instruments are now available in the tropics, a region undergoing rapid changes in terms of
885 human activity and emissions of ozone precursors. The present study takes advantage of these
886 new data records to assess the distribution of tropical tropospheric ozone, and it uses the longest
887 records to assess its trends:

888 Present-day distribution

- 889 ● With greater availability of ozone profiles across the tropics we can now demonstrate that
890 southern India is among the most polluted regions (Western Africa, tropical South
891 Atlantic, Southeast Asia, Malaysia/Indonesia) with 95th percentile ozone values reaching
892 80 nmol mol⁻¹ in the lower free troposphere, comparable to mid-latitude regions, such as
893 Northeast China/Korea.
- 894 ● The lowest ozone values (5th percentile) are less than 10 nmol mol⁻¹, and are observed by
895 SHADOZ and ATom in the boundary layer (below 700 hPa) above the Americas and the
896 tropical South Pacific.
- 897 ● From space, the distribution of tropical tropospheric column ozone (TTCO) varies among
898 the satellite products by 5-10 DU in the 20°S-20°N latitude band.
- 899 ● The satellite data tend to overestimate tropical ozone with mean biases (between the
900 surface and 270 hPa) ranging between 0 for IASI/GOME2 and 9 DU for
901 OMPS/MERRA2 when compared to IAGOS, ATom and SHADOZ.
- 902 ● The smallest biases (≤ 2 DU) are found when matching the top limit of the in situ profiles
903 to that of the OMI, TROPOMI and IASI/GOME2 satellite records.
- 904 ● The in situ observations were critical for adjusting the biases in the satellite products,
905 bringing them into closer alignment. The TTOB is about 31.5 Tg in both tropical
906 hemispheres up to 15°N or 15°S. The TTOB is larger in the northern hemisphere than in
907 the southern hemisphere by about 2 Tg when considering the larger latitude band
908 between 20°S and 20°N. The seasonal variability of TTOB is weaker closer to the equator
909 in the northern hemisphere.

910 Trends

- 911 ● When focusing on the longest available records exceeding 20 years (1994-2019,
912 IAGOS/SHADOZ data reported in this study) or 30 years (1979-2016 satellite record
913 reported by Ziemke et al., 2019) we see a consistent picture of increasing ozone across
914 the tropics. IAGOS and SHADOZ data were fused to increase the sample sizes and to
915 improve the statistics of the data over three out of the five IAGOS regions: Americas,
916 Southeast Asia, Malaysia/Indonesia (Western Africa and India with no SHADOZ data).
917 India and Malaysia/Indonesia are the regions with the strongest ozone increase below 800
918 hPa (11 ± 2.4 and 8 ± 0.8 nmol mol⁻¹ decade⁻¹ close to the surface, respectively) and India
919 above 400 hPa (up to 6.8 ± 1.8 nmol mol⁻¹ decade⁻¹). Southeast Asia and
920 Malaysia/Indonesia show the highest increase in the mid-troposphere (550-750 hPa, up to
921 3.4 ± 0.8 and 4 ± 0.5 nmol mol⁻¹ decade⁻¹, respectively). Trends of the tropical
922 tropospheric column ozone reflect these results. In terms of in situ trend reliability based
923 on data availability and *p*-value of trend estimate, we have the most confidence in



924 Western Africa (while it is still not ideal due to moderate data gaps) and the least
925 confidence in Samoa and Americas.

- 926 ● For shorter time periods (< 20 years) trend detection can be even more challenging due to
- 927 the larger additional uncertainty associated with sparsely sampled ozone records.
- 928 ● The OMI and OMI/MLS satellite records have a very high sampling frequency compared
- 929 to the sparse in situ datasets and mostly show positive 15-year (2004-2019) trends above
- 930 the IAGOS regions (from 0.55 ± 1.22 to 2.31 ± 1.34 nmol mol⁻¹ decade⁻¹) with the
- 931 maximum trends over Southeast Asia of 2.31 ± 1.34 nmol mol⁻¹ decade⁻¹ with OMI CCD,
- 932 and 1.69 ± 0.89 nmol mol⁻¹ decade⁻¹ with OMI/MLS. The strongest agreement between
- 933 satellite and in situ trends is found above Southeast Asia where TTCO had increased at a
- 934 rate of about 2-3 nmol mol⁻¹ decade⁻¹. These trends are consistent with the results from
- 935 Ziemke et al. (2019) using TOMS-OMI/MLS records and Gaudel et al. (2020) using
- 936 IAGOS ozone profiles. Above the other regions, we only have low to medium confidence
- 937 in the in situ trends, therefore we concluded that we have no reason to reject the positive
- 938 tropical tropospheric ozone trends based on satellite data. However, the discrepancy
- 939 between the weak positive satellite trends and the weak negative in situ trends above
- 940 Natal + Ascension Island warrants further investigation.

941

942 This study demonstrates that most tropical regions require either an increased and/or
943 continuous sampling (in situ and remote sensing) of ozone because either there are no data, or
944 the data are so sparse that it is difficult to estimate accurate and precise trends to evaluate the
945 satellite records. However, we also demonstrate that the current sampling frequency is adequate
946 for bias correcting the satellite products, as shown in Figure 8.

947 TROPOMI, IASI/GOME2, CrIS and OMPS/MERRA2 are recently available satellite
948 records and their overlap for several years with the OMI record will assure continuity of ozone
949 and precursors observations from space when the NASA Aura mission terminates by 2025.
950 GEMS, the only geostationary mission covering the tropics (tropical Asia), will bring new
951 capabilities in monitoring the region with the strongest ozone increases in the world, with higher
952 spatial and temporal resolution than the polar orbiting instruments.

953 This study underscores the importance of developing TTCO data with a common
954 definition of the top of the tropospheric column. Additionally, there is a pressing need for the
955 availability of common or joint retrievals for satellite data, such as those provided by initiatives
956 like TROPES (TROpospheric Ozone and its Precursors from Earth System Sounding,
957 <https://tes.jpl.nasa.gov/tropes/>).

958 Moreover, to better understand the drivers behind the observed increases in TTOB, it is
959 essential to conduct simulations using global chemical transport models, chemistry climate
960 models, Earth system models, and regional models spanning recent decades. Encouragingly,
961 these endeavors have been newly proposed within the framework of the Tropospheric Ozone
962 Assessment Report phase II (TOAR-II), an initiative under the International Global Atmospheric
963 Chemistry (IGAC) project. These efforts will be the focus of forthcoming publications featured
964 in the TOAR-II Community Special Issue.

965



966 **Appendix A**

967

968 The Intergovernmental Panel on Climate Change (IPCC) developed a guidance note for the
969 consistent treatment of uncertainties (Mastrandrea et al., 2010) that was followed by the fifth and
970 sixth IPCC assessment reports. Among other applications, the calibrated language described by
971 the guidance note is helpful for the discussion of long-term trends and for communicating the
972 level of confidence that an author team wishes to assign to a particular trend value, or to an
973 ensemble of trend values. Confidence in the validity of a finding is expressed qualitatively with
974 five qualifiers (very low, low, medium, high and very high), based on the type, amount, quality,
975 and consistency of the available evidence, and the level of agreement among studies addressing
976 the same phenomenon (see Figure 1 of Mastrandrea et al., 2010).

977 Following IPCC, the Tropospheric Ozone Assessment Report (TOAR) developed its own
978 guidance note on best statistical practices for TOAR analyses, featuring an uncertainty scale for
979 assessing the reliability and likelihood of the estimated trend (Chang et al., 2023). The
980 uncertainty scale has five qualifiers as follows: very low certainty or no evidence, low certainty,
981 medium certainty, high certainty and very high certainty. Each qualifier corresponds to a range
982 of values associated with either the signal-to-noise ratio or the p -value of the trend. A limitation
983 of the uncertainty scale is that it is best suited for surface ozone time series with high frequency
984 sampling, which allows for robust calculation of monthly means, upon which the trends are
985 calculated. For the case of calculating trends based on sparse ozone profiles, in many cases the
986 monthly means are biased or unreliable due to low sampling frequency, which adds additional
987 uncertainty to the calculation of the trend. Because the p -value (or the signal-to-noise ratio) of a
988 trend based on monthly means does not consider the impact of low sampling frequency on the
989 monthly means, we developed new calibrated language to express our confidence in trends based
990 on sparse ozone profiles.

991 Following the methodology of IPCC (Mastrandrea et al., 2010) Table A1 presents a
992 confidence scale that we use in this present study to express our confidence in a trend based on
993 sparse ozone profiles (as reported in Table 1 in the main text). Any line fit through a time series
994 will produce a trend value that is either positive or negative, and we use this scale to answer the
995 question: “Are we confident that a positive or negative trend is reliable?”. The confidence scale
996 considers both data coverage (based on the number of profiles per month and continuity of
997 sampling) and the estimation of the uncertainty of the trend, based on the p -value and the 95%
998 confidence interval. Higher confidence can be placed on trends with lower p -values and greater
999 data coverage, while less confidence is placed on trends with relatively high p -values and low
1000 data coverage. The selection of a particular confidence level is qualitative, with no sharp
1001 boundaries, however the following guidelines inform our decision-making:

1002 **Data coverage:** Previous studies (Logan, 1999; Saunois et al. 2012; Chang et al., 2020) have
1003 shown that sampling rates of once per week (or less) fail to provide accurate monthly means,
1004 while increased sampling rates of 2 or 3 times per week are more accurate. The most accurate
1005 sampling rate is 4 times per week or higher. Continuous data records with no, or limited gaps,
1006 are more reliable than records with multiple or large gaps. Data length also plays a role in trend



1007 reliability. A time series with more than 90% of months with data, and with more than 15
 1008 profiles per month is considered to have high data coverage. A time series with 66 to 90% of
 1009 months with data, and with 7-15 profiles per month is considered to have moderate data coverage
 1010 (this also applies to a region that only meets one condition for high data coverage). A time series
 1011 that has less than 66% of months with data, or less than 7 profiles per month has low data
 1012 coverage. It should be noted that, based on our criteria, none of the current study regions meet
 1013 the criteria for high data coverage, and therefore the top row in Table A1 is not applicable to this
 1014 study. In addition, since we derive the trends based on either a 25-year or a 15-year record, it is
 1015 natural to consider the trends derived from a longer data record are more robust, as a record
 1016 length less than two decades is generally insufficient to eliminate the impact of interannual
 1017 variability (Weatherhead et al., 1998; Barnes et al., 2016; Fiore et al., 2022). Therefore, all of the
 1018 time series in Table 1 with 15-year records are considered to have low data coverage.

1019 **Estimation uncertainty:** In general, lower *p*-values and higher signal-to-noise ratios are
 1020 indicators of a robust trend. The “Guidance note on best statistical practices for TOAR analyses”
 1021 (Chang et al., 2023) assigns the following degrees of certainty according to *p*-value: very high
 1022 certainty ($p \leq 0.01$), high certainty ($0.05 \geq p > 0.01$), medium certainty ($0.10 \geq p > 0.05$), low
 1023 certainty ($0.33 \geq p > 0.10$), very low certainty or no evidence ($p > 0.33$). We acknowledge that
 1024 the trends calculation does not consider the inherent quality of the data (i.e. accuracy and
 1025 precision of the data), which will be explore in future studies within TOAR Phase II.

1026

1027

1028 **Table A1.** Calibrated language for discussing confidence in long-term trend estimates based on
 1029 ozone profiles. Data coverage refers to the number of ozone profiles in a month, and the number
 1030 of months with available data. Estimation uncertainty refers to the uncertainty of a trend line
 1031 drawn through monthly means, as quantified by the *p*-value and the 95% confidence interval.

↑ Data coverage (based on the number of profiles per month and continuity of sampling)	medium confidence low estimation certainty high data coverage	high confidence moderate estimation certainty high data coverage	very high confidence high estimation certainty high data coverage
	low confidence low estimation certainty moderate data coverage	medium confidence moderate estimation certainty moderate data coverage	high confidence high estimation certainty moderate data coverage
	very low confidence or no evidence low estimation certainty low data coverage	low confidence moderate estimation certainty low data coverage	medium confidence high estimation certainty low data coverage
Estimation uncertainty → (based on <i>p</i> -value)			

1032

1033

1034

<https://doi.org/10.5194/egusphere-2023-3095>

Preprint. Discussion started: 22 January 2024

© Author(s) 2024. CC BY 4.0 License.



1035

1036



1037 **Author contributions**

1038 Conception and design of the study: AG, IB, ML, K-LC, OC

1039 Generation, collection, assembly, analysis and/or interpretation of data: AG, IB, ML, K-LC, OC

1040 JZ, BS, AMT, RS, DEK, NS, DH, AK, JC, K-PH, PV, KA, JP, CT, TBR

1041 Drafting and/or revision of the manuscript: AG, IB, ML, K-LC, OC, JP, KA, AMT, RS, DH,

1042 AK, NS, JZ, GJF, BCM

1043 All authors approved for submission of the manuscript.

1044

1045

1046 **Competing interests**

1047 ORC is the Scientific Coordinator of the TOAR-II Community Special Issue, to which this paper

1048 has been submitted, but he is not involved with the anonymous peer-review process of this or

1049 any of the other papers submitted to the Special Issue journals.

1050

1051

1052



1053

1054 **Acknowledgements**

1055 This research was supported by the NOAA Cooperative Agreement with CIRES,
1056 NA17OAR4320101 and NA22OAR4320151.

1057 We acknowledge the support of the NOAA JPSS PGRR program.

1058 The authors acknowledge the strong support of the European Commission, Airbus and the
1059 airlines (Lufthansa, Air France, Austrian, Air Namibia, Cathay Pacific, Iberia and China
1060 Airlines, so far) who have carried the MOZAIC or IAGOS equipment and performed the
1061 maintenance since 1994. In its last 10 years of operation, MOZAIC has been funded by INSU-
1062 CNRS (France), Météo-France, Université Paul Sabatier (Toulouse, France) and the Jülich
1063 Research Center (FZJ, Jülich, Germany). IAGOS (<https://www.iagos.org/>) has been additionally
1064 funded by the EU projects IAGOS-DS and IAGOSERI. The IAGOS database is supported by
1065 AERIS, the French portal for data and service for the atmosphere (see [https://iagos.aeris-
1066 data.fr](https://iagos.aeris-
1066 data.fr), last access: April 2023). SHADOZ data are provided through support of NASA's Upper
1067 Atmospheric Composition (UACO), NOAA/Global Monitoring Division and operators and data
1068 archivists across 20 organizations in North and South America, Europe, Africa and Asia.

1069

1070 **Data Availability**

1071 The monthly quasi-biennial oscillation values can be found at [https://www.geo.fu-
1072 berlin.de/met/ag/strat/produkte/qbo/qbo.dat](https://www.geo.fu-
1072 berlin.de/met/ag/strat/produkte/qbo/qbo.dat).

1073 The monthly El Niño-Southern Oscillation index can be found
1074 at <https://psl.noaa.gov/enso/mei/>.

1075 ATom data are archived at https://daac.ornl.gov/ATOM/guides/ATom_merge.html and
1076 are published through the Distributed Active Archive Center for Biogeochemical Dynamics
1077 (Wofsy et al., 2018).

1078 IAGOS ozone profiles can be found at <https://iagos.aeris-data.fr/>.

1079 SHADOZ ozone profiles can be found at <https://tropo.gsfc.nasa.gov/shadoz/> (see
1080 reference list).

1081 IASI+GOME2 satellite data can be found at https://iasi.aeris-data.fr/o3_iago2/, last
1082 access 08/02/2023.

1083 OMI CCD, OMI/MLS and OMPS/MERRA2 can be found at [https://acd-
1084 ext.gsfc.nasa.gov/Data_services/cloud_slice/](https://acd-
1084 ext.gsfc.nasa.gov/Data_services/cloud_slice/).

1085 TROPOMI CCD can be found at NASA EarthData
1086 repository: <https://disc.gsfc.nasa.gov/datasets?keywords=tropomi&page=1>

1087 CrIS can be found at <https://disc.gsfc.nasa.gov/> (see the Method section for more details
1088 on the data preprocessing)

1089

1090



1091 **References**

1092

1093 Archibald, A.T. et al.: Tropospheric Ozone Assessment Report: A critical review of changes in
1094 the tropospheric ozone burden and budget from 1850 to 2100. *Elementa: Science of the*
1095 *Anthropocene*, 8(1), doi:10.1525/elementa.2020.034, 2020.

1096

1097 Barnes, E.A., Fiore, A.M. and Horowitz, L.W.: Detection of trends in surface ozone in the
1098 presence of climate variability. *Journal of Geophysical Research: Atmospheres*, 121(10),
1099 pp.6112-6129, 2016.

1100

1101 Blot, R., Nédélec, P., Boulanger, D., Wolff, P., Sauvage, B., Cousin, J.-M., Athier, G., Zahn, A.,
1102 Obersteiner, F., Scharffe, D., Petetin, H., Bennouna, Y., Clark, H., and Thouret, V.:
1103 Internal consistency of the IAGOS ozone and carbon monoxide measurements for the last
1104 25 years, *Atmos. Meas. Tech.*, 14, 3935–3951, [https://doi.org/10.5194/amt-14-3935-](https://doi.org/10.5194/amt-14-3935-2021)
1105 2021, 2021.

1106

1107 Bourgeois, I., Peischl, J., Thompson, C.R., Aikin, K.C., Campos, T., Clark, H., Commane, R.,
1108 Daube, B., Diskin, G.W., Elkins, J.W. and Gao, R.S.: Global-scale distribution of ozone
1109 in the remote troposphere from the ATom and HIPPO airborne field missions.
1110 *Atmospheric Chemistry and Physics*, 20(17), pp.10611-10635, 2020.

1111

1112 Bourgeois, I., Peischl, J., Thompson, C. R., Aikin, K. C., Campos, T., Clark, H., Commane, R.,
1113 Daube, B., Diskin, G. W., Elkins, J. W., Gao, R.-S., Gaudel, A., Hintsä, E. J., Johnson, B.
1114 J., Kivi, R., McKain, K., Moore, F. L., Parrish, D. D., Querel, R., Ray, E., Sánchez, R.,
1115 Sweeney, C., Tarasick, D. W., Thompson, A. M., Thouret, V., Witte, J. C., Wofsy, S. C.,
1116 and Ryerson, T. B.: Global-scale distribution of ozone in the remote troposphere from the
1117 ATom and HIPPO airborne field missions, *Atmos. Chem. Phys.*, 20, 10611–10635,
1118 <https://doi.org/10.5194/acp-20-10611-2020>, 2020.

1119

1120 Buonaccorsi, J. P.: Measurement error: models, methods, and applications. CRC press.
1121 Cochran, W. G. (1968). Errors of measurement in statistics. *Technometrics*, 10(4), 637-666,
1122 2010.

1123

1124 Chandra S, Ziemke, JR and Min, W et al.: Effects of 1997–1998 El Niño on tropospheric ozone
1125 and water vapor. *Geophys Res Lett*, 25:3867–70, 1998.

1126

1127 Chang, K. L., Cooper, O. R., Gaudel, A., Petropavlovskikh, I., & Thouret, V.: Statistical
1128 regularization for trend detection: an integrated approach for detecting long-term trends from
1129 sparse tropospheric ozone profiles. *Atmospheric Chemistry and Physics*, 20(16), 9915-9938,
1130 2020

1131

1132 Chang, K. L., Schultz, M. G., Lan, X., McClure-Begley, A., Petropavlovskikh, I., Xu, X., &
1133 Ziemke, J. R.: Trend detection of atmospheric time series: Incorporating appropriate
uncertainty estimates and handling extreme events. *Elem Sci Anth*, 9(1), 00035, 2021.



- 1134
1135 Chang, K. L., Cooper, O. R., Gaudel, A., Allaart, M., Ancellet, G., Clark, H., ... & Torres, C.:
1136 Impact of the COVID-19 Economic Downturn on Tropospheric Ozone Trends: An
1137 Uncertainty Weighted Data Synthesis for Quantifying Regional Anomalies Above Western
1138 North America and Europe. *AGU Advances*, 3(2), e2021AV000542, 2022.
1139
1140 Chang, K.-L., M. G. Schultz, G. Koren and N. Selke: Guidance note on best statistical practices
1141 for TOAR analyses. Available at: <https://igacproject.org/activities/TOAR/TOAR-II>, 2023.
1142
1143 Cooper, O. R., J. R. Ziemke, and K.-L. Chang: Tropospheric Ozone [in "State of the Climate in
1144 2021"]. *Bull. Amer. Meteor. Soc.* 103 (8), S96–S98, <https://doi.org/10.1175/BAMS-D-22-0092.1>, 2022.
1145
1146 Craigmile, P. F., & Guttorp, P.: A combined estimate of global temperature. *Environmetrics*,
1147 e2706, 2021.
1148
1149
1150 Cuesta, J., Eremenko, M., Liu, X., Dufour, G., Cai, Z., Höpfner, M., von Clarmann, T., Sellitto,
1151 P., Forêt, G., Gaubert, B. and Beekmann, M.: Satellite observation of lowermost tropospheric
1152 ozone by multispectral synergism of IASI thermal infrared and GOME-2 ultraviolet
1153 measurements over Europe. *Atmospheric Chemistry and Physics*, 13(19), pp.9675-9693,
1154 2013.
1155
1156 Davis, S.M., Hegglin, M.I., Fujiwara, M., Dragani, R., Harada, Y., Kobayashi, C., Long, C.,
1157 Manney, G.L., Nash, E.R., Potter, G.L. and Tegtmeier, S.: Assessment of upper
1158 tropospheric and stratospheric water vapor and ozone in reanalyses as part of S-
1159 RIP. *Atmospheric Chemistry and Physics*, 17(20), pp.12743-12778, 2017.
1160
1161 DeMazière, M., Thompson A. M., Kurylo, M. J., Wild, J., Bernhard, G., Blumenstock, T.,
1162 Hannigan, J., Lambert, J-C., Leblanc, T., McGee, T., Nedoluha, G., Petropavlovskikh, I.,
1163 Seckmeyer, G., Simon, P. C., Steinbrecht, W., Strahan, S., and Sullivan, J. T.: The
1164 Network for the Detection of Atmospheric Composition Change (NDACC): History,
1165 status and perspectives, *Atmos. Chem. Phys.*, acp-2017-402, 2018.
1166
1167 Doherty RM, Stevenson DS, Johnson CE, Collins WJ, Sanderson MG: Tropospheric ozone and
1168 El Niño–Southern Oscillation: Influence of atmospheric dynamics, biomass burning
1169 emissions, and future climate change. *J. Geophys. Res* **111**: D19304.
1170 doi:10.1029/2005JD006849, 2006.
1171
1172 Doniki, S., Hurtmans, D., Clarisse, L., Clerbaux, C., Worden, H. M., Bowman, K. W., and
1173 Coheur, P.-F.: Instantaneous longwave radiative impact of ozone: an application on
1174 IASI/MetOp observations, *Atmos. Chem. Phys.*, 15, 12971–12987,
1175 <https://doi.org/10.5194/acp-15-12971-2015>, 2015.
1176



- 1177 Elshorbany, Y. Y, H. C. Kapper, J. R. Ziemke, S. A. Parr, The Status of Air Quality in the
1178 United States during the COVID-19 Pandemic: A Remote Sensing Perspective, *Rem.*
1179 *Sens.*, 13(3), 369, <https://doi.org/10.3390/rs13030369>, 2021.
1180
- 1181 Feng, X., He, X., & Hu, J.: Wild bootstrap for quantile regression. *Biometrika*, 98(4), 995-999,
1182 2011.
1183
- 1184 Fleming, Z. L., R. M. Doherty, E. von Schneidmesser, C. S. Malley, et al.: Tropospheric Ozone
1185 Assessment Report: Present-day ozone distribution and trends relevant to human health,
1186 *Elem Sci Anth*, 6(1):12, DOI: <https://doi.org/10.1525/elementa.273>, 2018.
1187
- 1188 Fiore, A.M., Jacob, D.J., Field, B.D., Streets, D.G., Fernandes, S.D. and Jang, C.: Linking ozone
1189 pollution and climate change: The case for controlling methane. *Geophysical Research*
1190 *Letters*, 29(19), pp.25-1, 2002.
1191
- 1192 Fiore, Arlene M., Sarah E. Hancock, Jean-François Lamarque, Gustavo P. Correa, Kai-Lan
1193 Chang, Muye Ru, Owen R. Cooper, Audrey Gaudel, Lorenzo M. Polvani, Bastien
1194 Sauvage and Jerry R. Ziemke: Understanding recent tropospheric ozone trends in the
1195 context of large internal variability: A new perspective from chemistry-climate model
1196 ensembles, *Environmental Research: Climate*, <https://doi.org/10.1088/2752-5295/ac9cc2>,
1197 2022.
1198
- 1199 Fischer, E.V., Jaffe, D.A. and Weatherhead, E.C.: Free tropospheric peroxyacetyl nitrate (PAN)
1200 and ozone at Mount Bachelor: potential causes of variability and timescale for trend
1201 detection. *Atmospheric Chemistry and Physics*, 11(12), pp.5641-5654, 2011.
1202
- 1203 Fishman, J., Minnis, P., and Reichle, H. G.: Use of satellite data to study tropospheric ozone in
1204 the tropics, *J. Geophys. Res.*, 91(D13), 14451– 14465, doi:[10.1029/JD091iD13p14451](https://doi.org/10.1029/JD091iD13p14451),
1205 1986.
1206
- 1207 Fishman, J., and Larsen, J. C.: Distribution of total ozone and stratospheric ozone in the tropics:
1208 Implications for the distribution of tropospheric ozone, *J. Geophys. Res.*, 92(D6), 6627–
1209 6634, doi:[10.1029/JD092iD06p06627](https://doi.org/10.1029/JD092iD06p06627), 1987.
1210
- 1211 Fishman, J., Watson, C. E., Larsen, J. C., and Logan, J. A.: Distribution of tropospheric ozone
1212 determined from satellite data, *J. Geophys. Res.*, 95(D4), 3599– 3617,
1213 doi:[10.1029/JD095iD04p03599](https://doi.org/10.1029/JD095iD04p03599), 1990.
1214
- 1215 Fishman, J., Brackett, V.G. and Fakhruzzaman, K.: Distribution of tropospheric ozone in the
1216 tropics from satellite and ozonesonde measurements. *Journal of atmospheric and*
1217 *terrestrial physics*, 54(5), pp.589-597, 1992.
1218



- 1219 Fishman, J., V. G. Brackett, E. V. Browell and W. B. Grant: Tropospheric ozone derived from
1220 TOMS/SBUV measurements during TRACE A, *J. Geophys. Res.*, 101(D19), or
1221 <https://agupubs.onlinelibrary.wiley.com/doi/abs/10.1029/95JD03576>, 1996.
- 1222 Gaudel, A., O. R. Cooper, et al.: Tropospheric Ozone Assessment Report: Present-day
1223 distribution and trends of tropospheric ozone relevant to climate and global atmospheric
1224 chemistry model evaluation, *Elem. Sci. Anth.*, 6(1):39, DOI:
1225 <https://doi.org/10.1525/elementa.291>, 2018.
1226
- 1227 Gaudel, A., Cooper, O.R., Chang, K.L., Bourgeois, I., Ziemke, J.R., Strode, S.A., Oman, L.D.,
1228 Sellitto, P., Nédélec, P., Blot, R. and Thouret, V.: Aircraft observations since the 1990s
1229 reveal increases of tropospheric ozone at multiple locations across the Northern
1230 Hemisphere. *Science Advances*, 6(34), p.eaba8272, 2020.
1231
- 1232 Griffiths, P.T. et al.: Tropospheric ozone in CMIP6 Simulations. *Atmospheric Chemistry and*
1233 *Physics*, 21(5), 4187–4218, doi:10.5194/acp21-4187-2021, 2021.
1234
- 1235 Grubbs, F. E.: Errors of measurement, precision, accuracy and the statistical comparison of
1236 measuring instruments. *Technometrics*, 15(1), 53-66, 1973.
- 1237 Gulev, S.K., P.W. Thorne, J. Ahn, F.J. Dentener, C.M. Domingues, S. Gerland, D. Gong, D.S.
1238 Kaufman, H.C. Nnamchi, J. Quaas, J.A. Rivera, S. Sathyendranath, S.L. Smith, B.
1239 Trewin, K. von Schuckmann, and R.S. Vose: Changing State of the Climate System. In
1240 *Climate Change 2021: The Physical Science Basis. Contribution of Working Group I to*
1241 *the Sixth Assessment Report of the Intergovernmental Panel on Climate Change*
1242 [Masson-Delmotte, V., P. Zhai, A. Pirani, S.L. Connors, C. Péan, S. Berger, N. Caud, Y.
1243 Chen, L. Goldfarb, M.I. Gomis, M. Huang, K. Leitzell, E. Lonnoy, J.B.R. Matthews,
1244 T.K. Maycock, T. Waterfield, O. Yelekçi, R. Yu, and B. Zhou (eds.)]. Cambridge
1245 University Press, Cambridge, United Kingdom and New York, NY, USA, pp. 287–422,
1246 doi:10.1017/9781009157896.004, 2021.
1247
- 1248 Heue, K-P, et al.: Trends of tropical tropospheric ozone from 20 years of European satellite
1249 measurements and perspectives for the Sentinel-5 Precursor. *Atmos. Meas. Tech.* 9:
1250 5037–5051. DOI: <https://doi.org/10.5194/amt-9-5037-2016>, 2016.
1251
- 1252 Hogan, K.B., Hoffman, J.S. and Thompson, A.M.: Methane on the greenhouse agenda. *Nature*,
1253 354, pp.181-182, 1991.
1254
- 1255 Hubert, D., Heue, K.P., Lambert, J.C., Verhoelst, T., Allaart, M., Compernelle, S., Cullis, P.D.,
1256 Dehn, A., Félix, C., Johnson, B.J. and Keppens, A.: TROPOMI tropospheric ozone
1257 column data: geophysical assessment and comparison to ozonesondes, GOME-2B and
1258 OMI. *Atmospheric Measurement Techniques*, 14(12), pp.7405-7433, 2021.
1259
- 1260 Hughes, I., & Hase, T.: Measurements and their uncertainties: a practical guide to modern error
1261 analysis. OUP Oxford, 2010.



- 1262 Jenkins, GS, Gueye, M, Drame, MS & Ndiaye, SA 2014: Evidence of a LNO_x influence on
1263 middle/upper troposphere ozone-mixing ratios at Dakar, senegal during Northern
1264 Hemisphere summer season, Atmospheric Science Letters, vol. 15, no. 3, pp. 195-203.
1265 <https://doi.org/10.1002/asl2.489>, 2014.
1266
- 1267 Kley, D., Crutzen, P.J., Smit, H.G.J., Vömel, H., Oltmans, S.J., Grassl, H. and Ramanathan, V.:
1268 Observations of near-zero ozone concentrations over the convective Pacific: Effects on
1269 air chemistry. Science, 274(5285), pp.230-233, 1996.
1270
- 1271 Koenker, R., & Hallock, K. F.: Quantile regression. Journal of Economic Perspectives, 15(4),
1272 143-156, 2001.
1273
- 1274 Krishnamurti, T.N., Sinha, M.C., Kanamitsu, M., Oosterhof, D., Fuelberg, H., Chatfield, R.,
1275 Jacob, D.J. and Logan, J.: Passive tracer transport relevant to the TRACE A
1276 experiment. Journal of Geophysical Research: Atmospheres, 101(D19), pp.23889-23907,
1277 1996.
1278
- 1279 Lannuque, V., Sauvage, B., Barret, B., Clark, H., Athier, G., Boulanger, D., Cammas, J.P.,
1280 Cousin, J.M., Fontaine, A., Le Flochmoën, E. and Nédélec, P.: Origins and characterization
1281 of CO and O₃ in the African upper troposphere. Atmospheric chemistry and physics, 21(19),
1282 pp.14535-14555, 2021.
1283
- 1284 Leventidou, E., Weber, M., Eichmann, K.-U., Burrows, J. P., Heue, K.-P., Thompson, A. M., and
1285 Johnson, B. J.: Harmonisation and trends of 20-year tropical tropospheric ozone data,
1286 Atmos. Chem. Phys., 18, 9189-9205, <https://doi.org/10.5194/acp-18-9189-2018>, 2018.
1287
- 1288 Liu, J., Strode, S. A., Liang, Q., Oman, L. D., Colarco, P. R., Fleming, E. L., et al.: Change in
1289 tropospheric ozone in the recent decades and its contribution to global total ozone, Journal of
1290 Geophysical Research: Atmospheres, 127, e2022JD037170.
1291 <https://doi.org/10.1029/2022JD037170>, 2022.
1292
- 1293 Logan, J. A.: An analysis of ozonesonde data for the troposphere: Recommendations for testing
1294 3-D models and development of a gridded climatology for tropospheric ozone, J. Geophys.
1295 Res.-Atmos., 104, 16115–16149, 1999.
1296
- 1297 Mastrandrea, M. D., Field, C. B., Stocker, T. F., et al.: Guidance note for lead authors of the
1298 IPCC Fifth Assessment Report on consistent treatment of uncertainties. Intergovernmental
1299 Panel on Climate Change. Available at
1300 https://www.ipcc.ch/site/assets/uploads/2017/08/AR5_Uncertainty_Guidance_Note.pdf,
1301 2010
1302
- 1303 Mead, M.I., Castruccio, S., Latif, M.T., Nadzir, M.S.M., Dominick, D., Thota, A. and Crippa, P.:
1304 Impact of the 2015 wildfires on Malaysian air quality and exposure: a comparative study of
1305 observed and modeled data. Environmental Research Letters, 13(4), p.044023, 2018.



- 1306
1307 Mills, G., H. Pleijel, C. S. Malley, B. Sinha, et al.: Tropospheric Ozone Assessment Report:
1308 Present-day tropospheric ozone distribution and trends relevant to vegetation, *Elem. Sci.*
1309 *Anth.*, 6(1):47, DOI: <https://doi.org/10.1525/elementa.302>, 2018.
1310
1311 Miyazaki, K., Bowman, K., Sekiya, T., Eskes, H., Boersma, F., Worden, H., Livesey, N., Payne,
1312 V.H., Sudo, K., Kanaya, Y. and Takigawa, M.: Updated tropospheric chemistry reanalysis
1313 and emission estimates, TCR-2, for 2005–2018. *Earth System Science Data*, 12(3), pp.2223-
1314 2259, 2020.
1315
1316 Moffat, R. J.: Describing the uncertainties in experimental results. *Experimental thermal and*
1317 *fluid science*, 1(1), 3-17, 1988.
1318
1319 N. R. Nalli et al., "Validation of Atmospheric Profile Retrievals from the SNPP NOAA-Unique
1320 Combined Atmospheric Processing System. Part 2: Ozone," in *IEEE Transactions on*
1321 *Geoscience and Remote Sensing*, vol. 56, no. 1, pp. 598-607, Jan. 2018, doi:
1322 10.1109/TGRS.2017.2762600, 2018.
1323
1324 Nédélec, P., Blot, R., Boulanger, D., Athier, G., Cousin, J.M., Gautron, B., Petzold, A., Volz-
1325 Thomas, A. and Thouret, V.: Instrumentation on commercial aircraft for monitoring the
1326 atmospheric composition on a global scale: the IAGOS system, technical overview of
1327 ozone and carbon monoxide measurements. *Tellus B: Chemical and Physical*
1328 *Meteorology*, 67(1), p.27791, 2015.
1329
1330 Nguyen, H. et al.: Spatio-temporal data fusion for very large remote sensing datasets,
1331 *Technometrics*, 56.2 (2014): 174-185, 2014.
1332
1333 Ogino, S.-Y., Miyazaki, K., Fujiwara, M., Nodzu, M. I., Shiotani, M., Hasebe, F., et al.: Cause of
1334 a lower-tropospheric high-ozone layer in spring over Hanoi. *Journal of Geophysical*
1335 *Research: Atmospheres*, 127, e2021JD035727. [https://doi-](https://doi-org.colorado.idm.oclc.org/10.1029/2021JD035727)
1336 [org.colorado.idm.oclc.org/10.1029/2021JD035727](https://doi-org.colorado.idm.oclc.org/10.1029/2021JD035727), 2022.
1337
1338 Oman, L. D., Douglass, A. R., Ziemke, J. R., Rodriguez, J. M., Waugh, D. W., and Nielsen, J.
1339 E.: The ozone response to ENSO in Aura satellite measurements and a chemistry-climate
1340 simulation, *J. Geophys. Res.*, 118, 965– 976, doi:[10.1029/2012JD018546](https://doi.org/10.1029/2012JD018546), 2013.
1341
1342 Oltmans, S.J., Johnson, B.J., Harris, J.M., Vömel, H., Thompson, A.M., Koshy, K., Simon, P.,
1343 Bendura, R.J., Logan, J.A., Hasebe, F. and Shiotani, M.: Ozone in the Pacific tropical
1344 troposphere from ozonesonde observations. *Journal of Geophysical Research:*
1345 *Atmospheres*, 106(D23), pp.32503-32525.
1346 <https://agupubs.onlinelibrary.wiley.com/doi/pdfdirect/10.1029/2000JD900834>, 2001.
1347



- 1348 Paton-Walsh Clare, Kathryn M. Emmerson, Rebecca M. Garland, Melita Keywood, Judith J.
1349 Hoelzemann, Nicolás Huneeus, Rebecca R. Buchholz, Ruhi S. Humphries, Katye Altieri,
1350 Julia Schmale, Stephen R. Wilson, Casper Labuschagne, Egide Kalisa, Jenny A. Fisher,
1351 Nicholas M. Deutscher, Pieter G. van Zyl, Johan P. Beukes, Warren Joubert, Lynwil
1352 Martin, Thumeka Mkololo, Cybelli Barbosa, Maria de Fatima Andrade, Robyn Schofield,
1353 Marc D. Mallet, Mike J. Harvey, Paola Formenti, Stuart J. Piketh, Gustavo Olivares: Key
1354 challenges for tropospheric chemistry in the Southern Hemisphere. *Elementa: Science of*
1355 *the Anthropocene* 4 January 2022; 10 (1): 00050. doi:
1356 <https://doi.org/10.1525/elementa.2021.00050>, 2022.
1357
- 1358 Pope R., et al.: Investigation of spatial and temporal variability in lower tropospheric ozone from
1359 RAL Space UV-Vis satellite products, *ACP*, in-press; submitted version:
1360 <https://doi.org/10.5194/egusphere-2023-1172>, 2023.
1361
- 1362 Rabinovich, S. G.: Measurement errors and uncertainties: theory and practice. Springer Science
1363 & Business Media, 2006.
- 1364 Saunio, M., Emmons, L., Lamarque, J.-F., Tilmes, S., Wespes, C., Thouret, V., and Schultz, M.:
1365 Impact of sampling frequency in the analysis of tropospheric ozone observations, *Atmos.*
1366 *Chem. Phys.*, 12, 6757–6773, 2012.
1367
- 1368 Sauvage, B., Thouret, V., Cammas, J.P., Gheusi, F., Athier, G. and Nédélec, P.: Tropospheric
1369 ozone over Equatorial Africa: regional aspects from the MOZAIC data. *Atmospheric*
1370 *Chemistry and Physics*, 5(2), pp.311-335, 2005.
1371
- 1372 Sauvage, B., Martin, R. V., van Donkelaar, A., Liu, X., Chance, K., Jaeglé, L., Palmer, P. I., Wu,
1373 S., and Fu, T.-M. (2007a) Remote sensed and in situ constraints on processes affecting
1374 tropical tropospheric ozone, *Atmos. Chem. Phys.*, 7, 815–838,
1375 <https://doi.org/10.5194/acp-7-815-2007>
1376
- 1377 Sauvage, B., Martin, R.V., Van Donkelaar, A. and Ziemke, J.R., (2007b) Quantification of the
1378 factors controlling tropical tropospheric ozone and the South Atlantic maximum. *Journal of*
1379 *Geophysical Research: Atmospheres*, 112(D11), <https://doi.org/10.1029/2006JD008008>, 2007.
- 1380
- 1381 Shaddick, G. et al.: Data integration for the assessment of population exposure to ambient air
1382 pollution for global burden of disease assessment, *Environmental Science & Technology*
1383 52.16 (2018): 9069-9078, 2018.
1384
- 1385 SHADOZ data, <https://doi.org/10.57721/SHADOZ-V06>
1386
- 1387 Singh, R.P. and Chauhan, A., 2020. Impact of lockdown on air quality in India during COVID-
1388 19 pandemic. *Air Quality, Atmosphere & Health*, 13, pp.921-928.
1389



- 1390 Skeie, R.B., Myhre, G., Hodnebrog, Ø., Cameron-Smith, P.J., Deushi, M., Hegglin, M.I.,
1391 Horowitz, L.W., Kramer, R.J., Michou, M., Mills, M.J. and Olivie, D.J., 2020: Historical
1392 total ozone radiative forcing derived from CMIP6 simulations. *Npj Climate and Atmospheric*
1393 *Science*, 3(1), p.32, 2020.
- 1394
1395 Smith, N., & Barnet, C. D.: Uncertainty Characterization and Propagation in the Community
1396 Long-Term Infrared Microwave Combined Atmospheric Product System
1397 (CLIMCAPS). *Remote Sensing*, 11(10), Article 10. <https://doi.org/10.3390/rs11101227>,
1398 2019.
- 1399
1400 Smith, N. and Barnet, C. D.: CLIMCAPS observing capability for temperature, moisture, and
1401 trace gases from AIRS/AMSU and CrIS/ATMS, *Atmos. Meas. Tech.*, 13, 4437–4459,
1402 <https://doi.org/10.5194/amt-13-4437-2020>, 2020.
- 1403
1404 Sounder SIPS, & Barnet, Chris. (2020a): Sounder SIPS: Suomi NPP CrIMSS Level 2
1405 CLIMCAPS Full Spectral Resolution: Atmosphere cloud and surface geophysical state
1406 V2 [Data set]. NASA Goddard Earth Sciences Data and Information Services
1407 Center. <https://doi.org/10.5067/62SPJFQW5Q9B>, 2020.
- 1408
1409 Sounder SIPS, & Barnet, Chris. (2020b). Sounder SIPS: JPSS-1 CrIS Level 2 CLIMCAPS:
1410 Atmosphere cloud and surface geophysical state V2 [Data set]. NASA Goddard Earth
1411 Sciences Data and Information Services
1412 Center. <https://doi.org/10.5067/LESQUBLWS18H>, 2020.
- 1413
1414 Stauffer, R. M., A. M. Thompson, J. C. Witte, Characterizing global ozonesonde profile
1415 variability from surface to the UT/LS with a clustering technique and MERRA-2 reanalysis,
1416 *J. Geophys. Res.*, 123, doi: 10.1002/2017JD028465, 2018.
- 1417
1418 Stauffer, R.M., Thompson, A.M., Kollonige, D.E., Witte, J.C., Tarasick, D.W., Davies, J.,
1419 Vömel, H., Morris, G.A., Van Malderen, R., Johnson, B.J. and Querel, R.R.: A post-2013
1420 dropoff in total ozone at a third of global ozonesonde stations: Electrochemical
1421 concentration cell instrument artifacts? *Geophysical Research Letters*, 47(11),
1422 p.e2019GL086791, 2020.
- 1423
1424 Stauffer, R. M., Thompson, A. M., Kollonige, D. E., Tarasick, D. W., Van Malderen, R., Smit,
1425 H. G. J., et al.: An examination of the recent stability of ozonesonde global network data
1426 Date Updated: 30 August 2022. *Earth and Space Science*, 9, e2022EA002459.
1427 <https://doi.org/10.1029/2022EA002459>, 2022.
- 1428
1429 Sterling, C. W., B. J. Johnson, S. J., Oltmans, H. G. J. Smit, A. Jordan, P. D., Cullis, E. G., Hall,
1430 A. M., Thompson, and J. C. Witte: Homogenizing and Estimating the Uncertainty in
1431 NOAA's Long Term Vertical Ozone Profile Records Measured with the Electrochemical
1432 Concentration Cell Ozonesonde, *Atmos. Meas. Tech.* [https://doi.org/10.5194/amt-2017-](https://doi.org/10.5194/amt-2017-397)
1433 [397](https://doi.org/10.5194/amt-2017-397), 2017.



- 1434
1435 Szopa, S., V. Naik, B. Adhikary, P. Artaxo, T. Berntsen, W.D. Collins, S. Fuzzi, L. Gallardo, A.
1436 Kiendler-Scharr, Z. Klimont, H. Liao, N. Unger, and P. Zanis, 2021: Short-Lived Climate
1437 Forcers. In *Climate Change 2021: The Physical Science Basis. Contribution of Working*
1438 *Group I to the Sixth Assessment Report of the Intergovernmental Panel on Climate*
1439 *Change* [Masson-Delmotte, V., P. Zhai, A. Pirani, S.L. Connors, C. Péan, S. Berger, N.
1440 Caud, Y. Chen, L. Goldfarb, M.I. Gomis, M. Huang, K. Leitzell, E. Lonnoy, J.B.R.
1441 Matthews, T.K. Maycock, T. Waterfield, O. Yelekçi, R. Yu, and B. Zhou (eds.)].
1442 Cambridge University Press, Cambridge, United Kingdom and New York, NY, USA, pp.
1443 817–922, doi:10.1017/9781009157896.008, 2021.
1444
- 1445 Tarasick, D., Galbally, I.E., Cooper, O.R., Schultz, M.G., Ancellet, G., Leblanc, T., Wallington,
1446 T.J., Ziemke, J., Liu, X., Steinbacher, M. and Staehelin, J.: Tropospheric Ozone
1447 Assessment Report: Tropospheric ozone from 1877 to 2016, observed levels, trends and
1448 uncertainties. *Elementa: Science of the Anthropocene*, 7, 2019.
1449
- 1450 Taylor, J. R., & Thompson, W.: An introduction to error analysis: the study of uncertainties in
1451 physical measurements (Vol. 2, pp. 193-200). Mill Valley, CA: University science books,
1452 1982.
- 1453 Thompson, A.M. and Cicerone, R.J., 1986a: Atmospheric CH₄, CO and OH from 1860 to 1985.
1454 *Nature*, 321(6066), pp.148-150, 1986.
1455
- 1456 Thompson, A.M. and Cicerone, R.J., 1986b: Possible perturbations to atmospheric CO, CH₄,
1457 and OH. *Journal of Geophysical Research: Atmospheres*, 91(D10), pp.10853-10864,
1458 1986.
1459
- 1460 Thompson, A.M., Pickering, K.E., McNamara, D.P., Schoeberl, M.R., Hudson, R.D., Kim, J.H.,
1461 Browell, E.V., Kirchhoff, V.W.J.H. and Nganga, D.: Where did tropospheric ozone over
1462 southern Africa and the tropical Atlantic come from in October 1992? Insights from
1463 TOMS, GTE TRACE A, and SAFARI 1992. *Journal of Geophysical Research:*
1464 *Atmospheres*, 101(D19), pp.24251-24278, 1996.
1465
- 1466 Thompson, A. M., Doddridge, B. G., Witte, J. C., Hudson, R. D., Luke, W. T., Johnson, J. E.,
1467 Johnson, B. J., Oltmans, S. J. and Weller, R.: A tropical Atlantic Paradox: Shipboard and
1468 satellite views of a tropospheric ozone maximum and wave-one in January–February
1469 1999, *Geophysical Research Letters*, 27(20), 3317–3320, doi:10.1029/1999GL011273,
1470 2000.
1471
- 1472 Thompson, A.M., Witte, J.C., McPeters, R.D., Oltmans, S.J., Schmidlin, F.J., Logan, J.A.,
1473 Fujiwara, M., Kirchhoff, V.W., Posny, F., Coetzee, G.J. and Hoegger, B.: Southern
1474 hemisphere additional Ozonesondes (SHADOZ) 1998–2000 tropical ozone climatology
1475 1. Comparison with Total ozone mapping spectrometer (TOMS) and ground-based
1476 measurements. *Journal of Geophysical Research: Atmospheres*, 108(D2), 2003.



- 1477
1478 Thompson, A. M., and et al.: Southern Hemisphere Additional Ozonesondes (SHADOZ) 1998–
1479 2000 tropical ozone climatology 2. Tropospheric variability and the zonal wave-one, J.
1480 Geophys. Res., 108, 8241, doi:[10.1029/2002JD002241](https://doi.org/10.1029/2002JD002241), D2, 2003.
1481
1482 Thompson, A. M., et al.: Southern Hemisphere Additional Ozonesondes (SHADOZ) ozone
1483 climatology (2005–2009): Tropospheric and tropical tropopause layer (TTL) profiles
1484 with comparisons to OMI-based ozone products, J. Geophys. Res., 117, D23301,
1485 doi:10.1029/2011JD016911, 2012.
1486
1487 Thompson, A.M., Witte, J.C., Sterling, C., Jordan, A., Johnson, B.J., Oltmans, S.J., Fujiwara,
1488 M., Vömel, H., Allaart, M., PETERS, A. and Coetzee, G.J.: First reprocessing of Southern
1489 Hemisphere Additional Ozonesondes (SHADOZ) ozone profiles (1998–2016): 2.
1490 Comparisons with satellites and ground-based instruments. Journal of Geophysical
1491 Research: Atmospheres, 122(23), pp.13-000, 2017.
1492
1493 Thompson, A. M., J. C. Witte, C., Sterling, A., Jordan, B. J., Johnson, S. J. Oltmans, ... Thiongo,
1494 K.: First reprocessing of Southern Hemisphere Additional Ozonesondes (SHADOZ)
1495 ozone profiles (1998-2016): 2. Comparisons with satellites and ground-based
1496 instruments. Journal of Geophysical Research: Atmospheres, 122, 13,000-13,025.
1497 <https://doi.org/10.1002/2017JD027406>, 2017.
1498
1499 Thompson, A.M., Stauffer, R.M., Wargan, K., Witte, J.C., Kollonige, D.E. and Ziemke, J.R.:
1500 Regional and Seasonal Trends in Tropical Ozone from SHADOZ Profiles: Reference for
1501 Models and Satellite Products. Journal of Geophysical Research: Atmospheres, 126(22),
1502 p.e2021JD034691, 2021.
1503
1504 Torres, O., Bhartia, P. K., Jethva, H., and Ahn, C.: Impact of the ozone monitoring instrument
1505 row anomaly on the long-term record of aerosol products, Atmos. Meas. Tech., 11, 2701–
1506 2715, <https://doi.org/10.5194/amt-11-2701-2018>, 2018.
1507
1508 Tsivlidou, M., Sauvage, B., Barret, B., Wolff, P., Clark, H., Bennouna, Y., Blot, R., Boulanger,
1509 D., Nédélec, P., Le Flochmoën, E. and Thouret, V.: Tropical tropospheric ozone and
1510 carbon monoxide distributions: characteristics, origins and control factors, as seen by
1511 IAGOS and IASI. Atmospheric Chemistry and Physics, pp.1-50,
1512 <https://doi.org/10.5194/acp-23-14039-2023>, 2023.
1513
1514 Veefkind, J., Aben, I., McMullan, K., Förster, H., de Vries, J., Otter, G., Claas, J., Eskes, H.,
1515 de Haan, J., Kleipool, Q., van Weele, M., Hasekamp, O., Hoogeveen, R., Landgraf, J.,
1516 Snel, R., Tol, P., Ingmann, P., Voors, R., Kruizinga, B., Vink, R., Visser, H., and
1517 Levelt, P.: TROPOMI on the ESA Sentinel-5 Precursor: A GMES mission for global
1518 observations of the atmospheric composition for climate, air quality and ozone layer
1519 applications, Remote Sens. Environ., 120, 70–
1520 83, <https://doi.org/10.1016/j.rse.2011.09.027>, 2012. [a](#), [b](#), [c](#)
1521



- 1522 Wang, H., Lu, X., Jacob, D. J., Cooper, O. R., Chang, K.-L., Li, K., Gao, M., Liu, Y., Sheng, B.,
1523 Wu, K., Wu, T., Zhang, J., Sauvage, B., Nédélec, P., Blot, R., and Fan, S.: Global
1524 tropospheric ozone trends, attributions, and radiative impacts in 1995–2017: an integrated
1525 analysis using aircraft (IAGOS) observations, ozonesonde, and multi-decadal chemical
1526 model simulations, *Atmos. Chem. Phys.*, 22, 13753–13782, [https://doi.org/10.5194/acp-
1527 22-13753-2022](https://doi.org/10.5194/acp-22-13753-2022), 2022.
1528
- 1529 Wargan, K., Labow, G., Frith, S., Pawson, S., Livesey, N., and Partyka, G.: Evaluation of the
1530 ozone fields in NASA’s MERRA-2 reanalysis. *Journal of Climate* 30, 8, 2961-2988,
1531 <https://doi.org/10.1175/JCLI-D-16-0699.1>, 2017.
1532
- 1533 Wargan, K., N. Kramarova, B. Weir, S. Pawson, and S. M. Davis: Toward a reanalysis of
1534 stratospheric ozone for trend studies: Assimilation of the Aura Microwave Limb Sounder
1535 and Ozone Mapping and Profiler Suite Limb Profiler data, *J. Geophys. Res.*,
1536 125, <https://doi.org/10.1029/2019JD031892>, 2020.
1537
- 1538 Weatherhead, E.C., Reinsel, G.C., Tiao, G.C., Meng, X.L., Choi, D., Cheang, W.K., Keller, T.,
1539 DeLuisi, J., Wuebbles, D.J., Kerr, J.B. and Miller, A.J.: Factors affecting the detection of
1540 trends: Statistical considerations and applications to environmental data. *Journal of
1541 Geophysical Research: Atmospheres*, 103(D14), pp.17149-17161, 1998.
1542
- 1543 Witte, J.C., Thompson, A.M., Smit, H.G., Fujiwara, M., Posny, F., Coetzee, G.J., Northam, E.T.,
1544 Johnson, B.J., Sterling, C.W., Mohamad, M. and Ogino, S.Y.: First reprocessing of
1545 Southern Hemisphere ADDitional OZonesondes (SHADOZ) profile records (1998–2015):
1546 1. Methodology and evaluation. *Journal of Geophysical Research: Atmospheres*, 122(12),
1547 pp.6611-6636, 2017.
1548
- 1549 Witte, J. C., Thompson, A. M., Smit, H. G. J., Vömel, H., Posny, F., & Stübi, R. :First
1550 reprocessing of Southern Hemisphere ADDitional OZonesondes profile records: 3.
1551 Uncertainty in ozone profile and total column. *Journal of Geophysical Research:
1552 Atmospheres*, 123, 3243–3268, 8. <https://doi.org/10.1002/2017JD027791>, 2018.
1553
- 1554 WMO/GAW Report 268, 2021. Ozonesonde Measurement Principles and Best Operational
1555 Practices: ASOPOS 2.0 (Assessment of Standard Operating Procedures for Ozonesondes)
1556 August 2021, edited by H. G. J. Smit and A. M. Thompson. Available at:
1557 https://library.wmo.int/index.php?lvl=notice_display&id=21986#.Y4iiRn3MJc8
1558
- 1559 Wofsy S.C. et al., ATom: Merged Atmospheric Chemistry, Trace Gases, and Aerosols. ORNL
1560 DAAC (2018). <https://doi.org/10.3334/ORNLDAAC/1909> (Accessed 1 May, 2023).
1561
- 1562 Xiong, X., Liu, X., Wu, W., Knowland, K.E., Yang, Q., Welsh, J. and Zhou, D.K.: Satellite
1563 observation of stratospheric intrusions and ozone transport using CrIS on
1564 SNPP. *Atmospheric Environment*, p.118956.
1565 <https://doi.org/10.1016/j.atmosenv.2022.118956>, 2022.
1566



- 1567 Xue, L., A. Ding, O. Cooper, X. Huang, W. Wang, D. Zhou, Z. Wu, A. McClure-Begley, I.
1568 Petropavlovskikh, M. O. Andreae, C. Fu: ENSO and Southeast Asian biomass burning
1569 modulate subtropical trans-Pacific ozone transport, National Science Review, nwaal32,
1570 <https://doi.org/10.1093/nsr/nwaa132>, 2020.
1571
- 1572 Yamasoe, M.A., Sauvage B., Thouret V., Nédélec P., Le Flochmoen E., Barret B.: Analysis of
1573 tropospheric ozone and carbon monoxide profiles over South America based on
1574 MOZAIC/IAGOS database and model simulations, Tellus B: Chemical and Physical
1575 Meteorology, 67:1, DOI: [10.3402/tellusb.v67.27884](https://doi.org/10.3402/tellusb.v67.27884), 2015.
1576
- 1577 Young, P. J., Archibald, A. T., Bowman, K. W., Lamarque, J.-F., Naik, V., Stevenson, D. S.,
1578 Tilmes, S., Voulgarakis, A., Wild, O., Bergmann, D., Cameron-Smith, P., Cionni, I.,
1579 Collins, W. J., Dalsøren, S. B., Doherty, R. M., Eyring, V., Faluvegi, G., Horowitz, L.
1580 W., Josse, B., Lee, Y. H., MacKenzie, I. A., Nagashima, T., Plummer, D. A., Righi, M.,
1581 Rumbold, S. T., Skeie, R. B., Shindell, D. T., Strode, S. A., Sudo, K., Szopa, S., and
1582 Zeng, G.: Pre-industrial to end 21st century projections of tropospheric ozone from the
1583 Atmospheric Chemistry and Climate Model Intercomparison Project (ACCMIP), Atmos.
1584 Chem. Phys., 13, 2063–2090, <https://doi.org/10.5194/acp-13-2063-2013>, 2013.
1585
- 1586 Zhang, Y., Cooper, O.R., Gaudel, A., Thompson, A.M., Nédélec, P., Ogino, S.Y. and West, J.J.:
1587 Tropospheric ozone change from 1980 to 2010 dominated by equatorward redistribution
1588 of emissions, Nature Geoscience, 9(12), pp.875-879, 2016.
1589
- 1590 Zhang, Y., West, J.J., Emmons, L.K., Flemming, J., Jonson, J.E., Lund, M.T., Sekiya, T., Sudo,
1591 K., Gaudel, A., Chang, K.L. and Nédélec, P.: Contributions of world regions to the global
1592 tropospheric ozone burden change from 1980 to 2010. Geophysical Research
1593 Letters, 48(1), p.e2020GL089184, 2021.
1594
- 1595 Ziemke, J. R., Chandra, S., and Bhartia, P. K.: Two new methods for deriving tropospheric
1596 column ozone from TOMS measurements: The assimilated UARS MLS/HALOE and
1597 convective-cloud differential techniques, J. Geophys. Res., 103, 22115–22127, 1998.
1598
- 1599 Ziemke, J. R., Chandra, S., and Bhartia, P. K.: A 25-year data record of atmospheric ozone from
1600 TOMS Cloud Slicing: Implications for trends in stratospheric and tropospheric ozone, J.
1601 Geophys. Res., 110, D15105, doi:10.1029/2004JD005687, 2005.
1602
- 1603 Ziemke, J.R., Chandra, S., Duncan, B.N., Froidevaux, L., Bhartia, P.K., Levelt, P.F. and Waters,
1604 J.W.: Tropospheric ozone determined from Aura OMI and MLS: Evaluation of
1605 measurements and comparison with the Global Modeling Initiative's Chemical Transport
1606 Model. Journal of Geophysical Research: Atmospheres, 111(D19), 2006.
1607
- 1608 Ziemke, J. R., Joiner, J., Chandra, S., Bhartia, P. K., Vasilkov, A., Haffner, D. P., Yang, K.,
1609 Schoeberl, M. R., Froidevaux, L., and Levelt, P. F.: Ozone mixing ratios inside tropical



- 1610 deep convective clouds from OMI satellite measurements, *Atmos. Chem. Phys.*,
1611 9, 573–583, doi:10.5194/acp-9-573-2009, 2009.
- 1612
- 1613 Ziemke, J. R., Chandra, S., Labow, G. J., Bhartia, P. K., Froidevaux, L., and Witte, J. C.: A
1614 global climatology of tropospheric and stratospheric ozone derived from Aura OMI and
1615 MLS measurements, *Atmos. Chem. Phys.*, 11, 9237–9251, doi:10.5194/acp-
1616 11-9237-2011, 2011.
- 1617
- 1618 Ziemke, J. R., and Chandra, S.: Development of a climate record of tropospheric and ozone from
1619 satellite remote sensing: Evidence of an early recovery of global stratospheric ozone,
1620 *Atmos. Chem. Phys.*, 12, 5737-5753, doi:10.5194/acp-12-5737-2012, 2012.
- 1621
- 1622 Ziemke, J. R., Douglass, A. R., Oman, L. D., Strahan, S. E., and Duncan, B. N.: Tropospheric
1623 ozone variability in the tropics from ENSO to MJO and shorter timescales, *Atmos. Chem.*
1624 *Phys.*, 15, 8037–8049, <https://doi.org/10.5194/acp-15-8037-2015>, 2015.
- 1625
- 1626 Ziemke, J. R., Oman, L. D., Strode, S. A., et al.: Trends in global tropospheric ozone inferred
1627 from a composite record of TOMS/OMI/MLS/OMPS satellite measurements and the
1628 MERRA-2 GMI simulation, *Atmos. Chem. Phys.*, 19, 3257–3269,
1629 <https://doi.org/10.5194/acp-19-3257-2019>, 2019.
- 1630
- 1631
- 1632
- 1633
- 1634